

A SEARCH FOR SQUARKS AND GLUINOS
WITH THE CMS DETECTOR

EDWARD MATTHEW LAIRD

A DISSERTATION
PRESENTED TO THE FACULTY
OF PRINCETON UNIVERSITY
IN CANDIDACY FOR THE DEGREE
OF DOCTOR OF PHILOSOPHY

RECOMMENDED FOR ACCEPTANCE
BY THE DEPARTMENT OF
PHYSICS
ADVISOR: CHRISTOPHER TULLY

APRIL 2012

© Copyright by Edward Matthew Laird, 2012.

All Rights Reserved

Abstract

A search for squarks and gluinos is conducted, using the Compact Muon Solenoid detector at the Large Hadron Collider, in events containing energetic jets and apparent missing energy. Analyzed are 1.1/fb of data collected during the 2011 run at 7 TeV. Backgrounds from the mis-measurement of known processes are strongly suppressed using a novel kinematic variable, and the rates of the remaining backgrounds are estimated using control samples.

The data are found to agree with expectations from the Standard Model. The results are interpreted within the Constrained Minimal Supersymmetric Standard Model, where equal squark and gluino masses below 1.1 TeV are excluded at 95% confidence level. The results are also interpreted within simplified supersymmetric models, for which upper limits on the production cross sections are determined as functions of the super-partner particle masses.

Contents

Abstract	iii
List of Figures	vii
List of Tables	xi
Acknowledgments	xiii
1 Introduction	1
1.1 The Standard Model	2
1.2 Supersymmetry	3
1.3 Experimental signature	7
2 The Experiment	9
2.1 The Large Hadron Collider	9
2.1.1 The machine	9
2.1.2 Collisions of high-energy protons	12
2.2 The Compact Muon Solenoid	14
2.2.1 The detector	14
2.2.2 Event reconstruction	18
2.2.3 Event simulation	20

3	Event Selection	23
3.1	Overview and search strategy	23
3.2	Event pre-selection	25
3.2.1	Data sample	25
3.2.2	Trigger and event quality requirements	25
3.2.3	Objects and vetoes	26
3.2.4	Jet-based requirements	27
3.3	Final event selection	27
3.3.1	α_T	27
3.3.2	Other	30
3.3.3	Selected sample	31
4	Background Constraints	36
4.1	W + jets and top pair production	36
4.1.1	Selection of $W \rightarrow \mu\nu$ events	37
4.1.2	Background estimation procedure	38
4.2	Z + jets with invisible Z decay	40
4.2.1	Selection of photon + jet events	40
4.2.2	Background estimation procedure	42
4.2.3	Background cross-check: Estimation of $W \rightarrow \mu\nu$ + jets sample	44
4.3	Tail fraction dependence upon visible transverse energy	45
4.3.1	EWK	46
4.3.2	QCD	48
5	Statistical Framework	52
5.1	Likelihood model	52
5.1.1	Hadronic sample	52
5.1.2	H_T evolution model	53

5.1.3	Electroweak control samples	53
5.1.4	Contributions from signal	54
5.1.5	Total likelihood	55
5.2	Limits	55
6	Results and Interpretation	58
6.1	Standard Model	58
6.2	CMSSM	63
6.3	Simplified Models	66
6.4	Summary	67
	Bibliography	70
	Index	79

List of Figures

1.1	The sparticle spectrum for the benchmark point LM6 (see Table 2.2). From [33].	7
1.2	Two example diagrams of sparticle production and decay, in which P represents a proton, q a quark, \tilde{g} a gluino, \tilde{q} a squark, and $\tilde{\chi}^0$ a neutralino. From [4].	8
2.1	The layout of the LHC. From [34, 35].	10
2.2	The daily peak instantaneous luminosity delivered to CMS during the 2010 (left) and 2011 (right) 7 TeV pp runs vs. day. From [36].	11
2.3	The total integrated luminosity delivered to and collected by CMS during the 2010 (left) and 2011 (right) 7 TeV pp runs vs. day. From [36].	12
2.4	Left: the cross sections (in nb) of various SM processes vs. center-of- mass energy in pp collisions (when $\sqrt{s} > 4$ TeV) and $p\bar{p}$ collisions (when $\sqrt{s} < 4$ TeV). From [38]. Right: The cross sections (in pb) of various SUSY processes vs. sparticle mass, for pp collisions at $\sqrt{s} = 7$ TeV. From [39].	13
2.5	Top: a perspective view of CMS, from [40]. Bottom: a view of one quadrant of CMS. The volume enclosing the tracker is shown in light red, the electromagnetic calorimeter in light green, the hadron calorime- ter in lavender, and the forward calorimeter in magenta. The muon detectors are labeled. From [41].	15

2.6	The relative p_T resolution for central jets, determined using di-jet p_T -asymmetry with the 2010 dataset. From [45].	20
3.1	The distribution of reconstructed H_T for 35/pb of data, after a basic pre-selection. The sample was fed by an H_T trigger that was determined to be fully efficient by 250 GeV (the start of the plot). Overlaid are the expectations from simulated Standard Model processes, as well as two example signal models from the CMSSM, described in Table 2.2. From [1].	24
3.2	The distributions of α_T observed in the 2010 run for di-jet events (left) and for ≥ 3 jet events (right), after pre-selection and requiring $H_T > 350$ GeV. Expectations from simulation are overlaid, and overflows are shown in the right-most bin. The shaded band depicts the uncertainty in the expectations from simulation due to finite MC statistics and to uncertainty in the modeling of the jet energy resolution and scale. From [1].	29
3.3	The observed distribution of α_T after all other cuts, for $H_T > 375$ GeV. For illustration, SM expectations from the simulation are overlaid; the shaded band represents the uncertainty from finite MC statistics. From [2].	31
3.4	The observed distributions of $\#L_T/\#E_T$, the minimum $\Delta\phi^*$ of the selected jets, and the number of jets after all selection criteria. For illustration, SM expectations from the simulation are overlaid; the shaded band represents the uncertainty from finite MC statistics.	32
3.5	A reconstruction-level display of the highest H_T event in the hadronic sample.	35
4.1	The distribution of α_T in the muon control sample. From [5].	38

4.2	Distribution of α_T (left) and N_{jets} (right) for the photon sample before the cut on α_T . From [5].	42
4.3	Left: The distribution (data) of \cancel{H}_T vs. photon p_T before the α_T cut; the black line is $y = x$. Right: the distribution of photon p_T after the α_T cut; overflows are displayed in the last bin.	43
4.4	Left: the dependence of R_{α_T} on H_T from simulated events. Right: the same dependence, when the cross sections of the EWK background components are individually varied by $\pm 15\%$. The markers are artificially offset for clarity. Modified from [5].	47
4.5	The observed dependence of R_{α_T} on H_T , as well as the prediction from the control samples for the total EWK background. The markers are artificially offset for clarity. Modified from [2].	48
4.6	R_{α_T} vs. H_T observed in 770/pb of data for the α_T sideband sample (left) and the background-enriched sample (right). Also shown are the results of fits using the functional forms described in the text.	49
5.1	The distributions of the test statistic for the example model LM6 under the two hypotheses; also shown is the observed value.	56
5.2	CL_s vs. $f[\times 1 \text{ pb}]$ for two different signal models, in this case pairs of $(m_{\text{gluino}}, m_{\text{LSP}})$ within the simplified model T1. The blue line segments indicate where the interpolated curves cross 0.05, <i>i.e.</i> the upper limits for the models' cross sections.	57
6.1	Observed yields and fit results in the hadronic (top), muon (bottom left), and photon (bottom right) samples. The signal model LM6 is stacked on the expected background for illustration only; it plays no role in the fit. From [5].	60
6.2	The correlation matrix of the fit parameters.	61

6.3	Fit results for the fraction of the EWK background which is $Z \rightarrow \nu\bar{\nu}$, <i>i.e.</i> the parameters <code>fZinv</code> . The nominal fit (left) and the alternate fit (right) agree within uncertainties. In the alternate fit, <code>fZinv0</code> and <code>fZinv7</code> float, and the intermediate variables are evaluated using linear interpolation.	62
6.4	Observed yields and ML expectations in the hadronic sample, with LM6 stacked for illustration, all divided by the observed “bulk” yields. Modified from [5].	62
6.5	The total production cross section as a function of m_0 and $m_{1/2}$ in the specified slice of the CMSSM. Models with coordinates in the white areas were not sampled.	63
6.6	The selection efficiency for points in the specified slice of the CMSSM. Models with coordinates in the white areas were not sampled.	64
6.7	Observed and expected limits in the specified slice of the CMSSM; models below the red curve are excluded at 95% C.L. Curves of constant gluino mass and of constant mean u, d, c, s squark masses are drawn as well. In the shaded gray region, the LSP is electrically charged, and hence the models do not exhibit a missing energy signature. From [2].	65
6.8	The analysis acceptance times efficiency for two simplified models: gluino pairs (left), and squark pairs (right). The dashed lines indicate where the neutralino mass is equal to the gluino mass (left) or squark mass (right). From [5].	67
6.9	95% C.L. upper limits on cross sections for simplified models: gluino pairs (left); squark pairs (right). The labeled curves indicate where the limit is below a computed cross section for the model. From [5].	68

List of Tables

2.1	The simulated Standard Model samples used, with hard processes generated by MadGraph (left) and PYTHIA (right). Cuts are in GeV.	21
2.2	The definition of the low mass (LM) CMSSM benchmark points used [32].	22
3.1	Jet thresholds used in the three regions of H_T . Numbers are in GeV.	27
3.2	Yields obtained in the hadronic sample with $H_T > 375$ GeV. The MC entries are scaled to 1.1/fb. Standard Model is the sum of QCD, $t\bar{t}$, $Z + \text{jets}$, and $W \rightarrow l\nu + \text{jets}$; the $t\bar{t}$ column contains also single top production; the $Z + \text{jets}$ column includes both $Z \rightarrow \nu\bar{\nu} + \text{jets}$ and Drell-Yan di-lepton production. A trigger requirement is not applied to the MC samples; hence the yields are comparable to data only in the last two rows, at which point requirements stricter than the trigger have been applied.	34
4.1	Muon sample predictions for 1.1/fb. From [5].	39
4.2	Variables and upper thresholds used for photon identification. From [68].	41
4.3	Photon sample predictions for 1.1/fb. From [5].	44
4.4	Predictions of $W + \text{two jets}$ events using the photon sample for 1.1fb^{-1} . From [5].	45

4.5	The event yields used in the numerator and denominator of R_{α_T} and the resulting values, in bins of H_T , for 1.1 fb^{-1} . In the lowest bin, R_{α_T} has been multiplied by 1.01 to account for trigger inefficiency. Also shown are the mean values of H_T computed from the events with $\alpha_T < 0.55$. From [5].	47
4.6	Yields obtained in the photon control sample with $H_T > 375 \text{ GeV}$. The MC entries are scaled to $1.1/\text{fb}$. MC total is the sum of QCD and $\gamma + \text{jets}$. Comparison of data and MC is possible after the horizontal line, when the applied cuts are stricter than the skim criteria used to obtain the input datasets (see text). A hyphen indicates that a given cut was not applied to a particular sample. The cuts that are not photon-specific are explained in Sections 3.2 and 3.3.	51
6.1	Comparison of the observed yields in the different H_T bins of the hadronic, $\mu + \text{jets}$, and $\gamma + \text{jets}$ samples with the expectations and uncertainties given by the simultaneous fit to the SM-only hypothesis. From [2].	59
6.2	The maximum-likelihood parameter values under the SM-only hypothesis, and their error estimates as given by HESSE.	61

Acknowledgments

First and foremost I thank my principal advisor, Chris Tully. His wisdom, guidance and patience have been invaluable. I thank Peter Meyers for introducing me to high energy physics and teaching me a tremendous amount about neutrino experiments and particle physics generally.

It has been a pleasure to work on this analysis together with (in alphabetical order) Rob Bainbridge, Burt Betchart, Oliver Buchmüller, Darren Burton, Henning Flücher, Zoë Hatherell, Bryn Mathias, Tatiana Medvedeva, Tanja Rommerskirchen, Paris Sphicas, Markus Stoye, and Tom Whyntie. I thank Lance Dixon for discussions of vector boson production at the LHC, and the HEP group at Imperial College London for the use of their computing resources.

The members of the CMS collaboration have designed, constructed, commissioned, operated, and maintained a fantastic instrument. It is an honor to have contributed alongside so many talented people with such diverse backgrounds and interests. I thank in particular those with whom I worked directly in the HCAL and SUSY groups, and especially Dick Kellogg, who was always generous with his time, knowledge, and coffee machine.

I congratulate the members of the CERN accelerator divisions on the outstandingly successful 2010 and 2011 LHC runs. CERN's hospitality and the funding agencies of the supporting governments have made LHC and CMS possible. I thank the members of the free software community, and in particular those who have built

GNU/Linux, ROOT, and Python, for their vision, dedication, and high-quality tools which were essential to this work.

Fellow physics students (in reverse chronological order) Burt Betchart, Davide Gerbaudo, Ryan Patterson, Joe Checkelsky, Willie Leight, and Andrew Lin have taught me far more than I can recall, both about physics and many other subjects. Pey-Yi Chu gave much wise advice, especially on completing a dissertation. I am grateful to my parents and siblings for their constant encouragement. Serge Lang taught me, in addition to a lot of mathematics, to process information and to think critically. This work is dedicated to his memory.

The work described in this dissertation has been published in two articles [1, 2] and three CMS physics analysis summaries [3, 4, 5], and has been supported by the U.S. Department of Energy.

Chapter 1

Introduction

The field of particle physics is considered by its practitioners to have reached a crossroads. The Standard Model provides a framework for understanding the wealth of results from accelerator- and cosmic ray-based experiments, in many cases with great precision. Nonetheless, significant pieces remain obscure: the mechanism of electroweak symmetry breaking and process of WW scattering, the (non-)existence of particles with masses of order 1 TeV, and, further from the frontiers of knowledge, the (non-)unification of the fundamental forces at very small distances and the possibility of their connection to gravity. In addition, the cosmological measurements of energy densities consistent with dark matter and dark energy hypotheses, while fitting into a phenomenological framework, have exposed a lack of understanding of the fundamental constituents of matter.

The physics goals of the experimental collaborations at the Large Hadron Collider—the largest project to date for the field—are precisely to elucidate the mechanism of electroweak symmetry breaking, to explore the TeV mass scale, and to seek a connection between the particles produced in proton collisions and dark matter. Described in this dissertation is one particular course of exploration: a search for hypothetical particles whose existence would offer a clue about what physics may lie beyond the

Standard Model. Used throughout is the system of units in which $\hbar = c = 1$.

1.1 The Standard Model

The set of known elementary particles, their properties, and their interactions are expressed in a quantum field theory called the Standard Model (SM) [6, 7, 8, 9, 10]. It is described in detail elsewhere (*e.g.* [11]), but a brief summary is given here. The SM contains three symmetries: SU(3) for color charge, SU(2) for weak isospin, and U(1) for weak hypercharge; requiring its Lagrangian to be invariant under local gauge transformations determines its structure.

It describes the electron (e), muon (μ), and tau (τ) leptons, all with spin 1/2 and electric charge -1, and their associated neutral, massless, spin-1/2 neutrinos ν_e , ν_μ , ν_τ . They are arranged into SU(2) doublets of weak isospin $(\nu_l, l)_L$ of left-handed states, and singlets l_R of right-handed states. Extending the SM to include massive neutrinos, as required by the observation of neutrino flavor oscillations, is discussed in *e.g.* [12].

The spin-1/2 quarks are similarly arranged into three “generations”: (u, d) , (c, s) , (t, b) , with electric charges $(+2/3, -1/3)$. They carry color charge, and their weak interactions take place among a set of states mixed by a rotation matrix. Quarks are not observed free, but rather understood as the elementary constituents of color-neutral composite hadrons.

The interactions among particles are mediated by spin-1 bosons: eight electrically neutral, massless gluons (carrying color charges); the neutral, massless photon γ ; the massive W^\pm and Z^0 . Spontaneous breaking of the electroweak SU(2) \times U(1) symmetry gives masses to the W and Z , and further gives rise to the neutral, spin-0 Higgs particle H^0 , with a positive vacuum expectation value. The SM contains 19 parameters [13], usually taken to be the three lepton masses, six quark masses,

four parameters characterizing generational mixing among the quarks, three coupling strengths, the masses of the Z and H , and a coefficient allowing for the violation of combined charge-conjugation and parity-inversion symmetry in strong interactions. (The description of neutrino mass requires additional parameters.)

The success of the SM at predicting and interpreting experimental results is tremendous: all of the leptons, quarks, and gauge bosons have been observed, and interact according to the SM at length scales down to approximately 10^{-18} m [14]. Despite its broad success, however, the SM remains incomplete: the nature of neutrino masses and their mixing is not yet determined; it is not known how to incorporate the observed dark matter (should it consist of particles), nor the effects of gravity, which are expected to become relevant at high energies.

Perhaps most importantly, the proposed mechanism of electroweak symmetry breaking, and in particular the existence of the scalar H , are not yet confirmed by experiment. In addition, its mass m_H is not predicted, and m_H^2 receives contributions via virtual particle loops that depend quadratically on the momentum cut-off used, *i.e.* the scale at which new physics shall enter the calculation. Assuming that m_H is $O(100 \text{ GeV})$, as is required for WW scattering to remain perturbative, then either (a) new physics enters at the scale of $O(1 \text{ TeV})$, or (b) some mechanism is required to remove this quadratic divergence, *e.g.* supersymmetry [15].

1.2 Supersymmetry

Supersymmetry (SUSY) is a symmetry relating fermions and bosons. A supersymmetry transformation converts bosonic states into fermionic ones, and vice versa; quantum field theories which have invariant actions under such a transformation are called supersymmetric [16, 17, 18, 19, 20, 21].

Such theories have several motivations. First, they can provide a mechanism for

removing the quadratic dependence of the Higgs mass on momentum cut-off [22, 23]: the contribution to divergent (loop) diagrams from each SM fermion (resp. boson) is canceled by an opposite-sign contribution from a new boson (resp. fermion). Second, they can enable at high energy scales a unification of the values of the coupling strengths for the electromagnetic, weak, and strong forces, thereby opening up the possibility of a further unified view of fundamental forces [14]. In addition to the above two theoretical motivations, supersymmetric models can predict massive stable particles which interact only weakly, thus providing candidates for dark matter [14, 24].

The simplest implementation of SUSY consistent with the SM is called the Minimal Supersymmetric Standard Model (MSSM) [25]. For each particle in the SM, it introduces a “super-partner” particle (sparticle) with the same electric charge, weak isospin, and color as its particle partner, but differing by half a unit of spin. In particular:

- each SM SU(2)-doublet for a lepton l , $(\nu_l, l)_L$, has two super-partner particles, both spin-0: a sneutrino $\tilde{\nu}_L^l$ and a slepton \tilde{l}_L ; each singlet l_R has a spin-0 super-partner \tilde{l}_R ;
- analogously, each quark-pair doublet $(q, q')_L$ has squark partners $\tilde{q}_L, \tilde{q}'_L$, and each singlet q_R has a partner \tilde{q}_R ;
- two spin-1/2 higgsino doublets $(\tilde{H}_u^+, \tilde{H}_u^0), (\tilde{H}_d^0, \tilde{H}_d^-)$, have as partners two spin-0 Higgs doublets $(H_u^+, H_u^0), (H_d^0, H_d^-)$;
- the spin-1 gauge bosons (before electroweak symmetry breaking) g, W^\pm, W^0, B^0 have spin-1/2 partners the gluino, winos, and bino $\tilde{g}, \tilde{W}^\pm, \tilde{W}^0, \tilde{B}^0$.

After electroweak symmetry breaking, three of the eight degrees of freedom of the two complex SU(2)_L-doublets of Higgs fields become the longitudinal modes of the Z^0

and W^\pm bosons, and five Higgs scalars remain: h^0 , H^0 , A^0 , H^\pm . Further, the neutral higgsinos and gauginos mix to form four neutralinos ($\tilde{\chi}_{i=1-4}^0$); the charged higgsinos and winos mix to form two charginos ($\tilde{\chi}_{i=1,2}^\pm$); in both cases the indices are chosen such that increasing index means increasing mass. A prediction of the MSSM is that, if the sparticles that contribute quantum corrections to the lightest Higgs (h^0) have masses less than approximately 1 TeV, then $m_{h^0} \lesssim 135$ GeV [15].

Interactions which violate baryon- or lepton-number can be included in the MSSM. Such interactions are eliminated by imposing the conservation of R-parity [26], defined for a (s)particle as

$$P_R = (-1)^{3(B-L)+2s} \quad ,$$

where B represents the baryon number, L the lepton number, and s the spin. $P_R = +1$ for all SM particles and for Higgs scalars; $P_R = -1$ for all sparticles. Its conservation has three important consequences: the lightest sparticle (LSP) is stable, each sparticle decays to an odd number of LSPs, and beams of colliding particles produce sparticles in even numbers. An LSP which interacts only weakly is of particular interest: if produced in a particle collision, it will escape direct detection and cause an apparent momentum imbalance among collision products.

The fact that no sparticles have been observed so far, and in particular not with masses equal to the corresponding SM particles, indicates that supersymmetry (should it hold) is not apparent in the ground state chosen, *i.e.* it is broken spontaneously. There is substantial freedom in how to break SUSY in the MSSM; after the requirements of gauge invariance, R-parity conservation, and maintenance of the cancelation of quadratic divergences, there remain ~ 100 free parameters representing masses, phases, and mixing angles [27].

A convenient approach to choosing values for these parameters is to adopt, in addition to those of the SM, only five parameters [28, 29]: a common mass for scalars

m_0 ; a common mass for gauginos $m_{1/2}$; a universal SUSY-breaking tri-linear coupling A_0 ; the ratio of vacuum expectation values of the two Higgs doublets $\tan \beta$, and the sign of a Higgsino mixing parameter $\text{sgn } \mu$. The first three parameters are fixed at the gauge coupling unification scale and are run down to the electroweak scale (M_Z) via renormalization group equations [30]. The resulting model is called the Constrained MSSM (CMSSM), and its five parameters determine the masses and couplings of all the sparticles. In particular [31, 32],

- $m_{\tilde{\chi}_1^0} \sim 0.45m_{1/2}$; $m_{\tilde{\chi}_2^0} \sim 2m_{\tilde{\chi}_1^0}$
- $m_{\tilde{g}} \sim 2.7m_{1/2}$
- $m_{\tilde{u}_L}^2 \sim m_0^2 + 5.0m_{1/2}^2 + 0.35M_Z^2 \cos 2\beta$
- $m_{\tilde{d}_L}^2 \sim m_0^2 + 5.0m_{1/2}^2 - 0.42M_Z^2 \cos 2\beta$
- $m_{\tilde{u}_R}^2 \sim m_0^2 + 4.5m_{1/2}^2 + 0.15M_Z^2 \cos 2\beta$
- $m_{\tilde{d}_R}^2 \sim m_0^2 + 4.4m_{1/2}^2 - 0.07M_Z^2 \cos 2\beta$

and similarly for \tilde{c} , \tilde{s} (though \tilde{t}_L and \tilde{t}_R mix, with the lower-mass eigenstate \tilde{t}_1 often lighter than all other squarks; \tilde{b}_L and \tilde{b}_R mix to some extent as well). The non-SM particles of an example CMSSM point are displayed in Figure 1.1.

At fixed values of the other parameters, there are three regions in the $m_{1/2}$ vs. m_0 plane which have different decay chains:

- The gluinos are heavier than any of the squarks. Then the decays proceed as $\tilde{g} \rightarrow \tilde{q}\bar{q}$, $\tilde{q} \rightarrow q\tilde{\chi}^0$, and the contribution of gluino production to the total squark/gluino production is smaller than that of squarks;
- The gluinos are heavier than some squarks but lighter than others. Then decays such as $\tilde{q}_L \rightarrow \tilde{g}q$, $\tilde{g} \rightarrow \tilde{b}\bar{b}$, $\tilde{b} \rightarrow b\tilde{\chi}^0$ are possible;

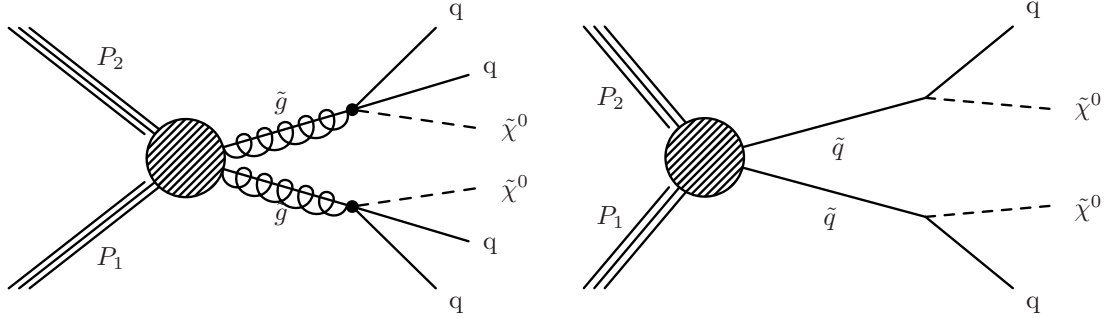


Figure 1.2: Two example diagrams of sparticle production and decay, in which P represents a proton, q a quark, \tilde{g} a gluino, \tilde{q} a squark, and $\tilde{\chi}^0$ a neutralino. From [4].

The observation of an excess of such events over SM expectations would not necessarily provide evidence for the principle of supersymmetry in particular. Many other interpretations could be possible. Nonetheless, supersymmetric theories provide a rich framework for interpretation. Two example schematic diagrams are shown in Figure 1.2: pair-produced gluinos, each decaying to two quarks and an escaping neutral particle; pair-produced squarks, each decaying to a quark and an escaping neutral particle. The color carried by the gluinos and squarks, and hence strong coupling to gluons and quarks comprising the incident protons, allows an appreciable production cross section. The differences in mass between the squarks/gluinos and the LSP allow the decay quarks to carry substantial energy. The escaping, undetected LSPs provide the apparent imbalance in transverse momentum.

Chapter 2

The Experiment

2.1 The Large Hadron Collider

2.1.1 The machine

CERN's Large Hadron Collider (LHC) is a storage ring, accelerator, and collider of circulating beams of protons or ions. It is housed in the tunnel dug for the Large Electron-Positron collider (LEP), approximately 27 km in circumference, 100 m underground, with bore-diameter 3.7 m, straddling the border between France and Switzerland outside of Geneva. It is described in detail elsewhere [34].

The LHC consists of two beam pipes which house counter-circulating beams and are merged in four sections around the ring to enable collisions of the beams. Each interaction point houses a large detector; the layout is shown in Figure 2.1. The remaining four straight sections contain acceleration, collimation, and beam dump systems. In the eight arc sections, the beam pipes are surrounded by superconducting dipole magnets, which are maintained at 2 K using superfluid helium and provide fields of up to 8 T to steer the beams. Magnets for focusing and corrections are also present in “short” straight sections within the arcs and near the interaction regions. The vacuum within the beam pipes is designed to maximize beam lifetime

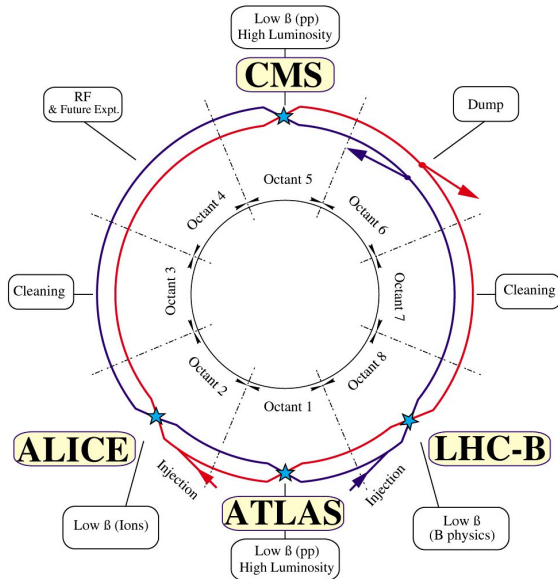


Figure 2.1: The layout of the LHC. From [34, 35].

and minimize interactions between the beams and residual gas molecules; it is under 10^{-10} mbar in the room-temperature sections near the experiments.

The protons (p) which form LHC’s beams are liberated from hydrogen molecules, accelerated in stages via a linear accelerator (Linac2) and three proton synchrotrons (PSB, PS, SPS) to 450 GeV, at which energy they are injected into the LHC ring, constituting a “fill”. The beams are ramped to full energy, squeezed, adjusted, and brought into collision. The transverse beam positions are scanned to maximize the pp collision rate, after which the beams are kept in collisions for ≥ 12 hours.

An LHC proton beam consists of many “bunches” *i.e.* approximately 1.1×10^{11} protons localized into less than 1 ns in the direction of motion. During the 2011 run, these bunches are spaced by 50 ns; there are up to approximately 1400 bunches per beam, with up to 1300 pairs colliding inside the CMS detector. The beams are ramped to 3.5 TeV per beam, requiring approximately 6 kA of current in the dipole magnets to produce a field strength of 4 T, and corresponding to $O(100)$ MJ of energy stored in the magnets. Each circulating beam-current is approximately 0.25 A, corresponding to another approximately 150 MJ stored in the beams. The performance

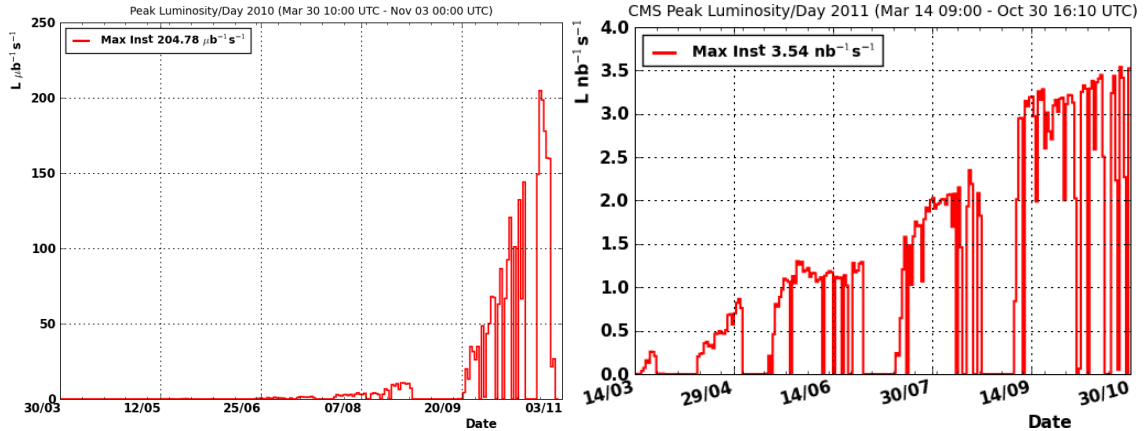


Figure 2.2: The daily peak instantaneous luminosity delivered to CMS during the 2010 (left) and 2011 (right) 7 TeV pp runs vs. day. From [36].

of the beam-dump and machine protection systems is thus critical.

The instantaneous luminosity of the machine, *i.e.* the rate of scattering events produced divided by the cross section of the process, is given by

$$L_{\text{inst}} = \frac{f n_b N_p^2}{A_{\text{eff}}} \quad (2.1)$$

where f is the orbit frequency (~ 11 kHz), n_b is the number of bunch pairs colliding, N_p is the number of protons per bunch, and A_{eff} is the effective area in which the bunches overlap, transverse to the beam directions.

The peak instantaneous luminosity per day at CMS for the 7 TeV runs is shown in Figure 2.2, and the luminosity integrated in Figure 2.3. In both figures, the scale of the vertical axis for the 2011 plot is a factor of 1000 larger than for the 2010 plot. The increase by orders of magnitude indicates both (a) the phenomenal success of LHC commissioning and running, and (b) the challenge presented to CMS to accommodate new running conditions nearly continuously, in particular to design and deploy suitable trigger tables, readout thresholds, reconstruction algorithms, and analysis methods.

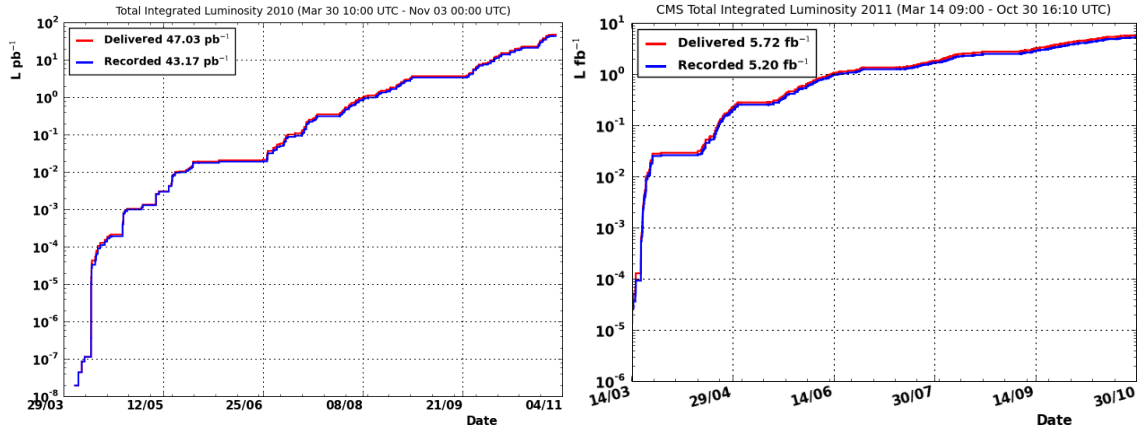


Figure 2.3: The total integrated luminosity delivered to and collected by CMS during the 2010 (left) and 2011 (right) 7 TeV pp runs vs. day. From [36].

2.1.2 Collisions of high-energy protons

A thorough description of the physics of hadron collisions can be found in [37]; some key aspects are mentioned briefly here. The interactions sought and the SM processes that appear as backgrounds are those in which substantial momentum is transferred between the constituent partons of the LHC's colliding protons; the incident protons are destroyed and energetic outgoing elementary particles and proton remnants are produced. The distributions of what fraction of a proton's momentum a constituent gluon or quark carries are given by parton distribution functions (PDFs). For a particular production process, *e.g.* $pp \rightarrow t\bar{t}$ or $pp \rightarrow \tilde{g}\tilde{g}$, there are various parton scattering processes, *e.g.* from initial gg or $q\bar{q}$, which contribute; their cross sections are integrated over momentum fraction according to the PDFs and summed to obtain a total production cross section.

Results of such cross section computations for a variety of processes are shown in Figure 2.4. The potentially tiny rate of sparticle production compared with that of known processes presents a challenge for the search. In addition, given the total inelastic cross section of order 50 mb, the luminosity per colliding pair of bunches achieved at the LHC is sufficiently high that the expected number of interactions that occur in the same crossing as an interaction of interest is non-negligible. For the data

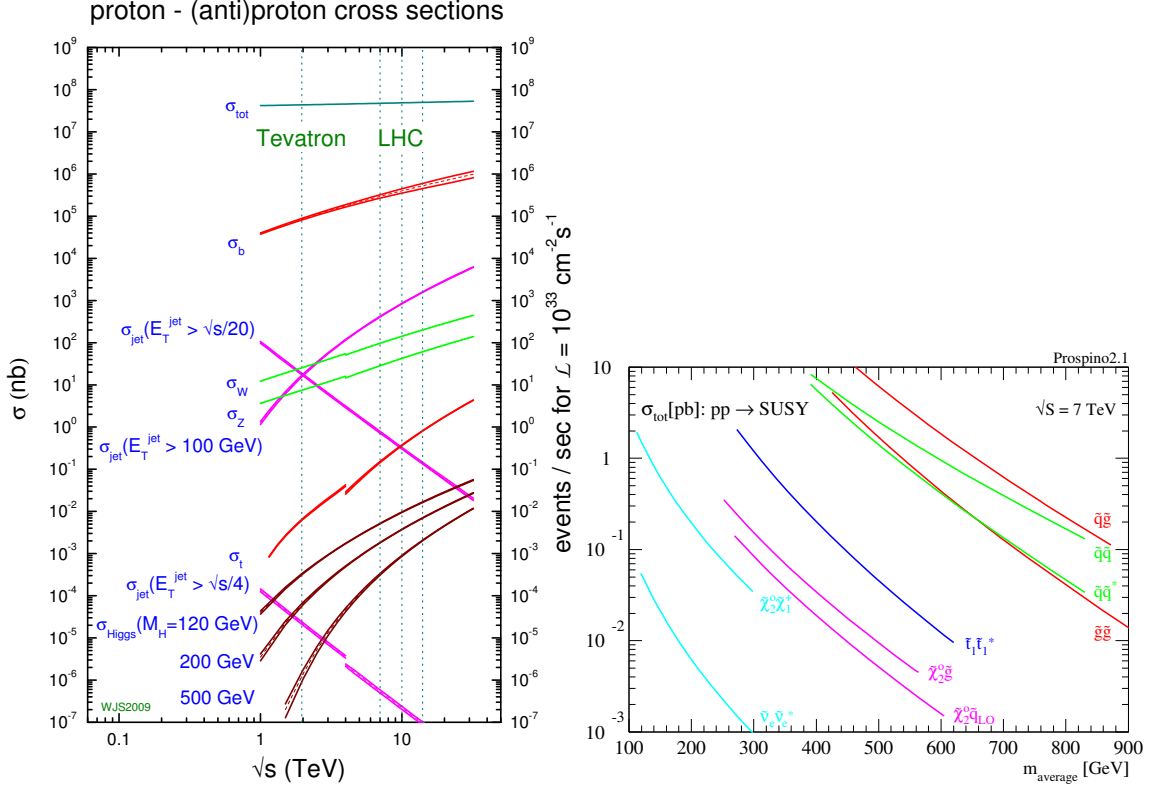


Figure 2.4: Left: the cross sections (in nb) of various SM processes vs. center-of-mass energy in pp collisions (when $\sqrt{s} > 4$ TeV) and $p\bar{p}$ collisions (when $\sqrt{s} < 4$ TeV). From [38]. Right: The cross sections (in pb) of various SUSY processes vs. sparticle mass, for pp collisions at $\sqrt{s} = 7$ TeV. From [39].

used in this search, the mean number of such “pile-up” interactions is approximately five.

Quarks or gluons which emerge from a hard-scattering process fragment and eventually group into hadrons before observation in a detector. They are visible as energetic sprays of hadrons called “jets”, which typically leave tracks in the inner detector and deposit energy in the calorimeters. The center-of-mass of the scattering system has a boost along the beam-line which varies event-by-event. It is therefore convenient to discuss jets (as well as other reconstructed particles) in terms of these quantities: transverse momentum p_T , which is invariant under such boosts, or similarly transverse energy $\equiv E \sin \theta$, with $0 \leq \theta \leq \pi$ the polar angle from the beam-line; and pseudo-rapidity $\eta \equiv -\ln \tan \theta/2$, of which differences are (approximately) invariant.

2.2 The Compact Muon Solenoid

2.2.1 The detector

The Compact Muon Solenoid (CMS) detector is designed to provide efficient identification and measurement of photons, electrons, muons, taus, and hadronic showers over wide ranges of transverse momentum and direction, and its nearly 4π coverage in solid angle provides accurate measurement of global transverse momentum imbalance. It has sufficient granularity to perform these measurements even when 10–20 interactions occur simultaneously in a collision of two bunches of protons, and fast enough response to do so when the time between beam crossings is 25 ns. Its components are resistant to damage from radiation, enabling its use to collect substantial luminosity, and its modularity allows for long-term maintenance and upgrades. When closed, CMS is a cylinder of length 22 m, diameter 15 m, and mass 12.5 kilotons. It is described in detail elsewhere [40].

The last name of the detector refers to a superconducting solenoid of radius 3 m and length 12.5 m, which carries 18 kA to provide a longitudinal magnetic field of 3.8 T. It is operated at 4.5 K. This magnet is surrounded by a central fixed “ring” and two movable rings on each side, constituting the “barrel”; it is flanked on each side by an “endcap”. The tracking system and calorimeters reside in the magnet bore. The layout is shown in the top plot of Figure 2.5. The x -axis is taken to point radially toward the center of the LHC ring, the y -axis to point against gravity, and the z -axis to form a right-handed coordinate system.

CMS is divided into “subdetector” systems, which perform complementary roles. The inner-most subdetector of the barrel consists of three layers of silicon pixel sensors that provide three-dimensional positions of the hit channels between 4 cm and 10 cm transverse to the beams. They are complemented by two endcap disks, enabling charged particles to leave typically three hits for pseudo-rapidity $|\eta| < 2.5$. Surround-

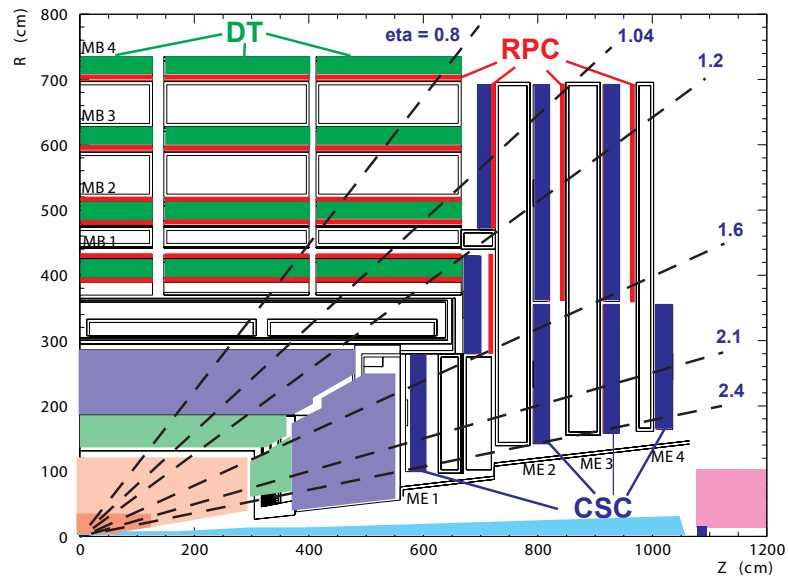
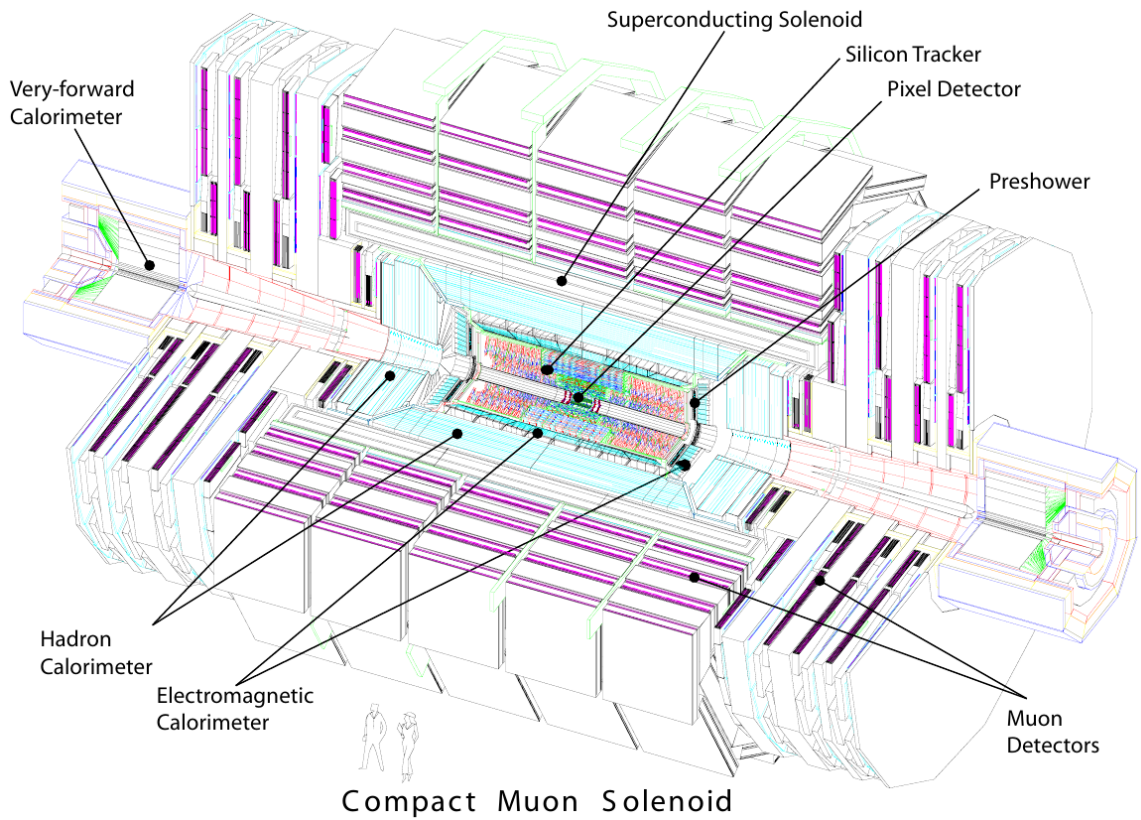


Figure 2.5: Top: a perspective view of CMS, from [40]. Bottom: a view of one quadrant of CMS. The volume enclosing the tracker is shown in light red, the electromagnetic calorimeter in light green, the hadron calorimeter in lavender, and the forward calorimeter in magenta. The muon detectors are labeled. From [41].

ing the pixel detector are ten layers of strips of silicon sensors out to 1.1 m, four of which have additional strips at a small stereo angle, allowing another dimension of hit position measurement. These are complemented by endcap disks as well. This tracking system provides efficient and precise determination of the charges, momenta, and impact parameters of charged particles.

Surrounding the tracker is an electromagnetic calorimeter (ECAL), consisting of scintillating PbWO_4 crystals of area 0.017×0.017 in $\Delta\eta \times \Delta\phi$ and length 23 cm, corresponding to about 25 radiation lengths. The crystals are instrumented with avalanche photo-diodes in the barrel ($|\eta| < 1.479$) and vacuum photo-triodes in the endcap ($1.479 < |\eta| < 3.0$). A lead-silicon sampling “pre-shower” detector is placed before the endcap to aid with the identification of neutral pions.

The hadron calorimeter (HCAL) consists of alternating layers of brass absorber and plastic scintillator, which sample hadronic showers, arranged in identical azimuthal units into two half-barrels and also into two endcaps. The scintillators are segmented projectively into towers of area $\Delta\eta \times \Delta\phi = 0.087 \times 0.087$ for $|\eta| < 1.6$, and approximately 0.17×0.17 for $|\eta| > 1.6$. The light produced in the scintillator layers is merged, wavelength-shifted and carried to the photo-cathode of a hybrid photo-diode (HPD). The single stage HPD accelerates the liberated electrons using a ~ 7 kV potential difference, which then impinge on a silicon diode. The current produced is amplified, digitized, and transmitted via optical links to dedicated boards. Coarse data, summed over longitudinal segments (which are present for $|\eta| > 1.2$) and time, are transmitted after peak-finding to the calorimeter trigger system. The full data, after the suppression of low energy hits to reduce data volume, are sent to the data acquisition system (DAQ).

Outside of the endcaps are forward calorimeters (HF) of steel absorber and quartz fibers, in which relativistic particles produce Cherenkov light. They cover the region $3.0 < |\eta| < 5.0$, thereby improving the hermeticity of CMS. Their hit-occupancy is

histogrammed at 40 MHz to track the delivered luminosity, and the instantaneous luminosity computed from the histograms is reported each “luminosity section”, *i.e.* 2^{18} beam orbits or approximately 23 seconds. The luminosity measurement is calibrated by scanning the transverse positions of the beams relative to each other to measure their effective overlap [42].

The magnet’s flux-return yoke and the endcaps are instrumented with muon detection systems, as shown in the bottom plot of Figure 2.5. The drift tube (DT), cathode strip chamber (CSC), and resistive plate chamber (RPC) systems provide efficient detection of muons with pseudo-rapidity $|\eta| < 2.4$. Further, they provide a muon trigger.

The CMS trigger system consists of two parts: “Level One” (L1), and “High Level” (HLT). The L1 is a set of electronics operating at 40 MHz, corresponding to the smallest achievable spacing between bunches in LHC, and has a latency of $3 \mu\text{s}$. In particular, in the trigger algorithms used in this work, coarse “trigger primitive” data from the electromagnetic and hadron calorimeters are streamed from the respective detectors. Neighboring projective towers are summed into regional transverse energies, from which electron/photon and jet candidate deposits are determined. If, in a particular time slice, at least one electron/photon candidate above a transverse energy threshold is found, or alternatively the sum of the transverse energies of the found jets exceeds a threshold, then a “Level One Accept” (L1A) signal is sent to the readout electronics of all subdetectors.

Upon receiving an L1A, approximately 600 boards transmit their event fragments via an optical network to a computer farm with approximately 1k nodes, which subsequently builds the events. The L1A rate is limited (by design) to 100 kHz, which at a luminosity of $2 \times 10^{33}/\text{cm}^2/\text{s}$ provides a rejection factor of approximately 200 for collisions within CMS. An additional 100 Hz of rate is used for a calibration sequence, in which subdetector channels are illuminated by laser and LED to measure drifts in

transparency and gain.

The HLT processes events with software reconstruction sequences that approximate the offline reconstruction as closely as possible, given the constraint on mean processing time of approximately 50 ms. The HLT provides a rejection factor of approximately 500 in order to achieve an event rate to disk of a few hundred per second. The recorded events are transferred from CMS to the CERN computing center, where event reconstruction is performed, and then distributed to CMS computing sites around the globe for storage and analysis.

During the 2010–2011 runs, nearly all components of CMS have performed according to design specifications. Most subdetectors have a stable fraction of functional channels between 97% and 99%, and the data-taking efficiency (by luminosity) is approximately 90%, as visible in Figure 2.3.

2.2.2 Event reconstruction

The goal of event reconstruction is to take the raw information recorded by the detector and to compute from it higher-level quantities which correspond roughly to properties of (a) individual particles, *e.g.* charge, momentum, or energy; (b) groups of particles produced in a shower, *e.g.* multiplicity or geometric profile; (c) the global event, *e.g.* total energy recorded, or degree of momentum balance. Many aspects of the reconstruction sequence are described in detail in [43]. Below is a brief description of those most relevant to this search.

The raw data read out from CMS are first converted to software representations of the digital samples of the detector signals, which are associated with individual detector elements. In a typical procedure, knowledge of pulse shapes, time-dependent channel-by-channel baseline values and gains, and detector geometry is then used to convert these samples into reconstructed “hits”, *i.e.* energy deposits in particular detector locations at particular times.

The reconstruction of particle tracks in the inner detectors proceeds in several steps: (a) seeds are determined from hits in the pixels layers; (b) approximate tracks are propagated outward, gathering matching hits and becoming more precise; (c) for each track a final fit is performed using all of its hits. Primary vertices are found by grouping tracks based on the z -coordinates of their points of closest approach to the beam-line, and for each cluster of tracks a fit is performed to determine the position of the vertex.

To identify and reconstruct muons, a trajectory is first determined using only the information from muon systems; then, if a matching track in the inner detector is found, a fit to the hits in both detectors is performed to determine the parameters of the muon trajectory. Such a muon is referred to as a “global” muon. This and other approaches are described in [41].

To reconstruct photons and electrons, hits in the ECAL are first clustered in rectangular strips of 5 crystals in η by 35 in ϕ (in the barrel), or one or more group of 5 by 5 crystals (in the endcaps) about energetic seed hits. Such a cluster contains nearly all of the energy in an electromagnetic shower, and serves already as a basic photon candidate. To reconstruct electrons, a trajectory from the measured cluster position is propagated inward to the pixel layers. If matching hits are found, they are used as a seed to build the electron track with a model that includes energy loss via radiation; the track and cluster are then used in tandem.

Jets are reconstructed using the anti- k_t algorithm [44] with size parameter $R = 0.5$. Input to the algorithm is the set of projective calorimeter towers with total deposited energy greater than approximately 1 GeV, which are treated as massless and with directions chosen to connect the tower center to the nominal interaction point. The raw jet energies are corrected to achieve a uniform relative response as a function of pseudo-rapidity, in particular to compensate for detector non-uniformities, and a calibrated absolute response as a function of transverse momentum [45]. The relative

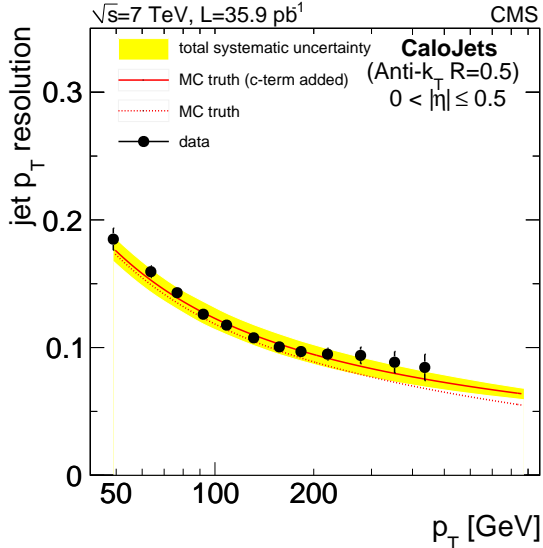


Figure 2.6: The relative p_T resolution for central jets, determined using di-jet p_T -asymmetry with the 2010 dataset. From [45].

p_T resolution for central jets, determined using di-jet p_T -asymmetry, is shown in Figure 2.6.

Missing transverse energy (\cancel{E}_T) is computed from the same towers of energy deposits in the calorimeters that are used for jet-finding; it is (minus) the vectorial sum of their components transverse to the beam-axis. Corrections are applied to accommodate the jet energy corrections and the presence of muons [46].

2.2.3 Event simulation

Simulated events (often called Monte Carlo or MC) are invaluable when designing and conducting a search. The relevant SM processes can be studied in detail, and even combined to provide a basic estimate of background rates. A simulated signal model allows a determination of the search efficiency, and makes interpretation of results within the model convenient.

In the generation of simulated events, partons from distribution functions (CTEQ [47] used by default) undergo hard scattering in MadGraph [48] or PYTHIA [49]; the outgoing partons shower, hadronize, and decay via PYTHIA. The resulting particles'

Table 2.1: The simulated Standard Model samples used, with hard processes generated by MadGraph (left) and PYTHIA (right). Cuts are in GeV.

Process	σ (pb)	QCD p_T bin	σ (pb)
$Z/\gamma^* \rightarrow l^+l^-$ ($m_{ll} > 50$)	3.05×10^3	30–50	5.31×10^7
$Z \rightarrow \nu\bar{\nu}$	5.72×10^3	50–80	6.36×10^6
$W \rightarrow l\nu$	3.13×10^4	80–120	7.84×10^5
$t\bar{t}$	1.58×10^2	120–170	1.15×10^5
t or \bar{t}	7.82×10^1	170–300	2.43×10^4
γ + jets ($40 < H_T < 100$)	3.00×10^4	300–470	1.17×10^3
γ + jets ($100 < H_T < 200$)	4.42×10^3	470–600	7.02×10^1
γ + jets ($200 < H_T$)	6.16×10^2	600–800	1.56×10^1
QCD ($100 < H_T < 250$)	8.89×10^6	800–1000	1.84×10^0
QCD ($250 < H_T < 500$)	2.17×10^5	1000–1400	3.32×10^{-1}
QCD ($500 < H_T < 1000$)	6.60×10^3	1400–1800	1.09×10^{-2}
QCD ($1000 < H_T$)	1.05×10^2	> 1800	3.58×10^{-4}

interactions in the detector and subsequent decays are simulated with a full description in GEANT [50], their energy deposits are digitized to emulate the response of the detector electronics, and event reconstruction is performed, as for data. Before digitization, hits from a number of simulated minimum-bias interactions are added to those of the “signal” event. The distribution of the number of simulated interactions overlaid is chosen to approximate LHC running conditions, and the MC events are subsequently reweighted so that the distribution of the number of reconstructed vertices has the same shape as the distribution in data.

The simulated Standard Model processes used are given in Table 2.1. The PYTHIA QCD samples were generated with the highest statistics, and for illustration are overlaid on the observed histograms shown in Chapter 3. Ratios of yields in the MadGraph samples are used in the background estimation, as described in Chapter 4. A “k”-factor of 1.27, determined by comparing the cross section for Z+jets production at NNLO and LO [51], has been applied to the MadGraph Z, γ , and QCD samples. The W and top cross sections are from [52].

Several CMSSM models have been generated with PYTHIA and fully simulated in the same fashion as the background samples; those used for illustration are listed in Table 2.2. Grids of signal points, in which parameters are scanned and at each value

Table 2.2: The definition of the low mass (LM) CMSSM benchmark points used [32].

Point	m_0 (GeV)	$m_{1/2}$ (GeV)	$\tan\beta$	A_0 (GeV)	$\text{sgn } \mu$
LM0	200	160	10	-400	+
LM1	60	250	10	0	+
LM4	210	285	10	0	+
LM6	85	400	10	0	+

many events generated, are used in Chapter 6. To process the large number of total events, a more approximate but substantially faster detector simulation is used for these grids [53].

Chapter 3

Event Selection

3.1 Overview and search strategy

The experimental signature of interest contains energetic jets, as mentioned in Section 1.3. The total visible transverse energy, H_T , is defined as the scalar sum of the transverse energies of the jets selected in an event, *i.e.* $\sum_j E_T^j$. The observed distribution of H_T is shown in Figure 3.1 for the 2010 dataset, and overlaid are the expectations from simulated Standard Model processes. It is apparent that for signal models like the examples shown, the background from SM multi-jet processes is overwhelming.

The search is designed to have a high rejection factor for inherently balanced multi-jet (“QCD”) events, including events with substantial mis-measurements of jet energy, or with an energetic neutrino within a jet, which can look like a mis-measurement. The separation of events with genuine and “fake” missing transverse energy is done primarily using a novel variable, α_T .

Events are selected which satisfy data quality requirements and have at least two energetic jets and no isolated electron or muon. Events are required to have $\alpha_T > 0.55$, which indicates the presence of escaping particle(s). Agreement is required between

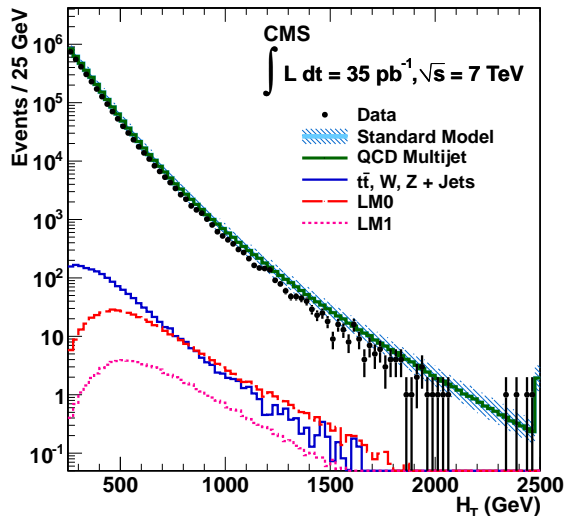


Figure 3.1: The distribution of reconstructed H_T for 35/pb of data, after a basic pre-selection. The sample was fed by an H_T trigger that was determined to be fully efficient by 250 GeV (the start of the plot). Overlaid are the expectations from simulated Standard Model processes, as well as two example signal models from the CMSSM, described in Table 2.2. From [1].

jet-based and calorimeter-tower-based missing transverse energy measurements, and events with evidence of severely mis-measured jets due to instrumental inefficiency are rejected.

The remaining SM background is composed predominantly of events from three processes that produce escaping neutrinos: $Z \rightarrow \nu\bar{\nu} + \text{jets}$, $W \rightarrow l\nu + \text{jets}$, and $t\bar{t}$ with at least one leptonic W decay. These backgrounds are constrained using two control samples containing events with either an isolated photon or muon. Signal models, on top of the data-driven background expectations, are tested for compatibility with the observed yields. The candidate events are binned in H_T , which in the presence of an excess could help to discriminate between possible models, and in any case improves the discrimination between signal and background when their distributions of H_T differ.

3.2 Event pre-selection

3.2.1 Data sample

The data considered have been collected from CMS run 160404 (March 13, 2011), until CMS run 167913 (June 28, 2011), corresponding after data quality requirements to an integrated luminosity of 1.1/fb ($\pm 4.5\%$) [42]. A few of the included figures use the data collected during the 2010 LHC Run, corresponding to a luminosity of 35/pb, and are labeled accordingly.

The collected data are reviewed run-by-run by a certification team, using (a) information from the detector control system, *e.g.* the current in the CMS magnet and the states of all sub-detector components; (b) histograms included in a “data quality monitoring” system, filled in real-time for a subset of collected events; (c) input from sub-detector and reconstruction experts, in particular the identification of transient problems such as a set of channels delivering no or scrambled data, or which is out-of-synchronization with the rest of the experiment. The granularity of certification is one luminosity section, and the fraction of data certified is approximately 90%.

3.2.2 Trigger and event quality requirements

The trigger path used requires the sum of the transverse energies of the jets found from the L1 calorimeter trigger primitives to exceed 100 GeV. At HLT, jets are reconstructed from the full calorimeter tower data; jets which have $p_T > 40$ GeV, $|\eta| < 3.0$, and satisfy loose identification requirements are used for further computation. The H_T is required to exceed 250 GeV. Further, the magnitude of the vectorial sum of the transverse momenta of the selected jets, *i.e.* $\cancel{H}_T \equiv |-\sum_j \vec{p}_T^j|$, is required to exceed a threshold of up to 90 GeV. The inefficiency of the trigger used, determined from a sample of events collected with an independent muon trigger, is approximately 1% after the full event selection.

The certified runs and ranges of luminosity sections are used. Further, several event quality requirements commonly used within CMS are imposed: “Stable Beams” asserted by LHC [54]; coincident signals from the clockwise and counter-clockwise beam pick-ups [55]; at least one well-reconstructed vertex within the nominal interaction region; at least 25% of reconstructed tracks have “good” quality; no evidence of spurious noise in the hadron calorimeter [56].

3.2.3 Objects and vetoes

Within the Standard Model, genuine \cancel{E}_T is caused by escaping neutrinos, which are produced in association with an electron, muon, or tau (lepton-number conservation). To reduce the rate of such events, any event which has (a) an isolated muon, as described in Section 4.1.1 with transverse momentum greater than 10 GeV; or (b) an isolated electron [57, 58] with transverse momentum greater than 10 GeV, is rejected. Events with an isolated photon with transverse momentum greater than 25 GeV are rejected to minimize overlap with dedicated photon-based searches at CMS [59, 60].

Events which contain energetic muons but are not vetoed above appear to have \cancel{E}_T when only the calorimeter deposits are considered; such events are handled as follows. If a global muon with transverse momentum greater than 10 GeV satisfies the identification requirements but not the isolation requirements listed in Section 4.1.1, and matches exactly one jet within a cone of $\Delta R < 0.5$, where $\Delta R \equiv \sqrt{\Delta\eta^2 + \Delta\phi^2}$, then the four-vector of the muon is added to that of the jet. If the muon matches multiple jets, or satisfies only loose identification criteria, then the event is rejected.

The jets used in the analysis are required to have transverse momentum $p_T > 50$ GeV and pseudo-rapidity $|\eta| < 3.0$. Further, in order to reject fake jets from calorimeter noise, jets are required to satisfy the “loose” quality criteria described in [61]. Any event which has a jet with $p_T > 50$ GeV that either fails these identification criteria or has $|\eta| > 3.0$, is rejected.

Table 3.1: Jet thresholds used in the three regions of H_T . Numbers are in GeV.

H_T range	min. p_T (any jet)	min. p_T (leading 2 jets)
$275 < H_T < 325$	36.7	73.3
$325 < H_T < 375$	43.3	86.7
$375 < H_T$	50.0	100.0

3.2.4 Jet-based requirements

Events are required to have at least two jets. The leading two jets are required each to have transverse momentum $p_T > 100$ GeV, and the leading jet to have $|\eta| < 2.5$. At low H_T , these thresholds are scaled down in order not to restrict phase space, and are listed in Table 3.1. An event which has $H_T < 375$ GeV when considering jets with $p_T > 50$ GeV, is rejected if it has $H_T > 375$ GeV when considering jets with $p_T > 43.3$ GeV, and likewise for the lower thresholds.

The magnitude of the vectorial sum of the transverse momenta of the selected jets, *i.e.* $\cancel{H}_T \equiv |-\sum_j \vec{p}_T^j|$, is required to exceed 100 GeV. This requirement is stricter than what is used in the trigger, and thus facilitates the comparison of data and simulation. It is superseded by the α_T cut, as explained in Section 3.3.1.

3.3 Final event selection

3.3.1 α_T

A novel kinematic variable, α , has been introduced by Randall and Tucker-Smith in [62] for a system of two jets, and defined as $p_T^{j_2}/m_{j_1 j_2}$, *i.e.* the transverse momentum of the second jet divided by the mass of the two-jet system. $\alpha_T^{\text{di-jet}} \equiv E_T^{j_2}/m_T$ has been presented in [63] as an alternative, *i.e.* the transverse energy of the second jet divided by the transverse mass of the system,

$$m_T \equiv \sqrt{\left(\sum_{i=1}^n E_T^{j_i}\right)^2 - \left(\sum_{i=1}^n p_x^{j_i}\right)^2 - \left(\sum_{i=1}^n p_y^{j_i}\right)^2} = \sqrt{H_T^2 - \cancel{H}_T^2} \quad (3.1)$$

(with $n = 2$). Or, alternatively,

$$\alpha_{\text{T}}^{\text{di-jet}} = \frac{E_{\text{T}}^{j_2}}{\sqrt{2E_{\text{T}}^{j_1}E_{\text{T}}^{j_2}(1 - \cos \Delta\phi_{j_1j_2})}} = \frac{\sqrt{E_{\text{T}}^{j_2}/E_{\text{T}}^{j_1}}}{\sqrt{2(1 - \cos \Delta\phi_{j_1j_2})}} \quad , \quad (3.2)$$

where $\Delta\phi_{j_1j_2}$ represents the difference in the azimuthal angles of the two (massless) jets. It is apparent in Equation 3.2 that for a system of jets which balance each other in the transverse plane, *i.e.* back-to-back and with equal transverse energies, then $\alpha_{\text{T}}^{\text{di-jet}} = 0.5$, whereas a mis-measurement of one of the transverse energies will cause $\alpha_{\text{T}}^{\text{di-jet}} < 0.5$. For jets which are not back-to-back, as is possible in events in which a W or Z recoils off a system of jets and decays to leptons, then $\alpha_{\text{T}}^{\text{di-jet}}$ can achieve values in excess of 0.5.

The distribution of $\alpha_{\text{T}}^{\text{di-jet}}$ after the pre-selection is shown in the left plot of Figure 3.2. The events were collected with an H_{T} trigger, and hence no cut on \cancel{H}_{T} is applied. The distribution falls over several orders of magnitude between 0.50 and 0.55, where a cut suppresses nearly all simulated QCD multi-jet events.

A particular extension of the definition of $\alpha_{\text{T}}^{\text{di-jet}}$ to events with more than two jets has been presented in [64]. The n selected jets are clustered into two ‘‘pseudo-jets’’, where each pseudo-jet’s transverse energy, E_{T}^{pj} , is defined as the scalar sum of the transverse energies of the constituent jets. Out of the 2^{n-1} possible configurations, the one is chosen for which the values of E_{T} for the two pseudo-jets match as closely as possible, *i.e.* the quantity $\Delta H_{\text{T}} \equiv |E_{\text{T}}^{pj_1} - E_{\text{T}}^{pj_2}|$ is minimized. Then, defining

$$\alpha_{\text{T}} \equiv \frac{1}{2} \frac{H_{\text{T}} - \Delta H_{\text{T}}}{m_{\text{T}}} \quad (3.3)$$

it is seen that for a system of two jets, α_{T} reduces to $\alpha_{\text{T}}^{\text{di-jet}}$, and using Equation 3.1, that

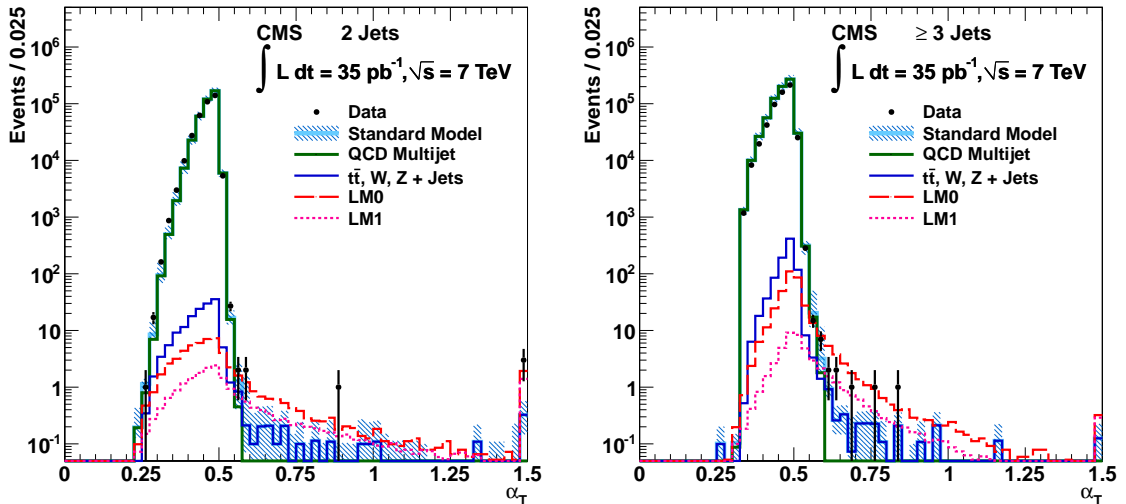


Figure 3.2: The distributions of α_T observed in the 2010 run for di-jet events (left) and for ≥ 3 jet events (right), after pre-selection and requiring $H_T > 350$ GeV. Expectations from simulation are overlaid, and overflows are shown in the right-most bin. The shaded band depicts the uncertainty in the expectations from simulation due to finite MC statistics and to uncertainty in the modeling of the jet energy resolution and scale. From [1].

$$\alpha_T = \frac{1}{2} \frac{H_T - \Delta H_T}{\sqrt{H_T^2 - \cancel{H}_T^2}} = \frac{1}{2} \frac{1 - \Delta H_T/H_T}{\sqrt{1 - (\cancel{H}_T/H_T)^2}} \quad (3.4)$$

The distribution of α_T for events with three or more jets is shown in the right plot of Figure 3.2, and is seen, as was the distribution of $\alpha_T^{\text{di-jet}}$, to fall sharply for $\alpha_T > 0.5$. Three curves of constant α_T (0.45, 0.50, 0.55) are drawn in the $\Delta H_T/H_T$ vs. \cancel{H}_T/H_T plot of Figure 3.5.

The requirement used in the search is $\alpha_T > 0.55$. Since the minimum possible value of ΔH_T is zero, one sees from Equation 3.4 that this requirement implies that $\cancel{H}_T/H_T > 0.416$. Thus the missing transverse momentum is required to be an appreciable fraction of the visible transverse energy (both quantities are computed from the jets alone). In particular, $\cancel{H}_T > 114$ GeV when $H_T > 275$ GeV, and hence the α_T cut supersedes the $\cancel{H}_T > 100$ GeV cut applied in the pre-selection.

3.3.2 Other

The requirement $\alpha_T > 0.55$ suppresses effectively the background from inherently balanced multi-jet events, even in the presence of moderate mis-measurement of jet E_T , or a jet which contains an energetic neutrino. Two effects have been identified which can cause multi-jet events to pass this requirement.

The first is the production of multiple low- p_T jets, with similar values of azimuthal angle ϕ , which are not accounted for because they fall below the p_T threshold used for selecting jets. Such events are rejected by requiring that the missing transverse momentum reconstructed from jets alone (\cancel{H}_T) not greatly exceed the missing transverse momentum reconstructed from all calorimeter towers (\cancel{E}_T): $\cancel{H}_T/\cancel{E}_T < 1.25$.

The second effect is the catastrophic mis-measurement of a jet's E_T if it enters one of a small number of geometric regions in the ECAL with non-functioning readout electronics. Such “dead” regions absorb electromagnetic showers but give no record of the energy deposited. A map is shown in the ϕ vs. η plot of Figure 3.5 (orange and magenta squares). The quantity

$$\Delta\phi_j^* \equiv \Delta\phi(\vec{p}_j, -\sum_{i \neq j} \vec{p}_i) \quad , \quad (3.5)$$

i.e. the angular separation in the transverse plane between a jet and the $\vec{\cancel{H}}_T$ computed without that jet, is evaluated for each identified jet from the set with $p_T > 30$ GeV. A small value is compatible with the hypothesis of an inherently balanced event in which a jet has been mis-measured. For each jet with $\Delta\phi_j^* < 0.5$, the number of dead ECAL cells within $\Delta R(\vec{p}_j, \text{cell}) < 0.3$ is counted. If the number exceeds 9 for any jet, then the event is rejected.

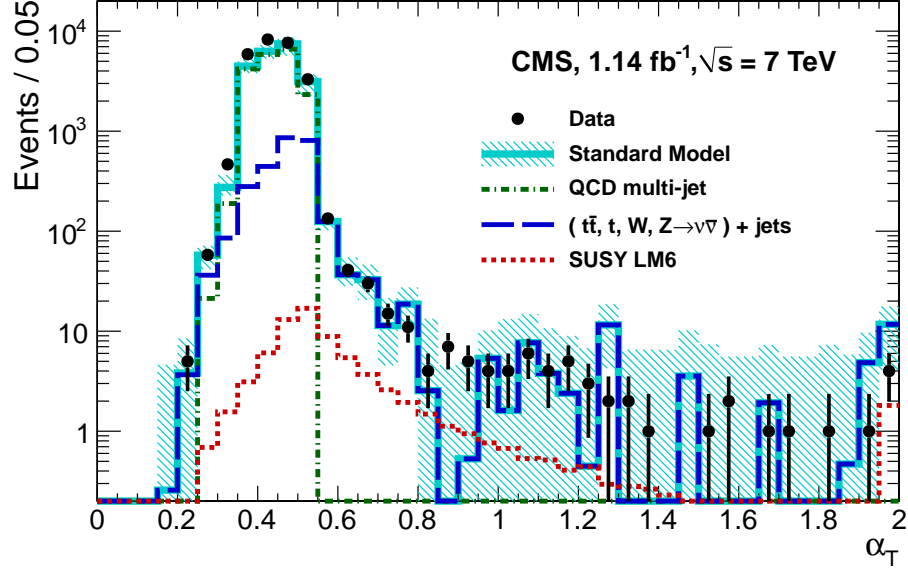


Figure 3.3: The observed distribution of α_T after all other cuts, for $H_T > 375$ GeV. For illustration, SM expectations from the simulation are overlaid; the shaded band represents the uncertainty from finite MC statistics. From [2].

3.3.3 Selected sample

After the full selection, the remaining SM events are expected to contain energetic escaping neutrinos from vector boson decays, in particular from $Z \rightarrow \nu\bar{\nu} + \text{jets}$, $W \rightarrow l\nu + \text{jets}$, and $t\bar{t}$ production (with the subsequent leptonic decay of a W). The event yields in data and, for illustration, in the relevant simulated samples are given in Table 3.2.

The distribution of α_T after all other cuts is shown in Figure 3.3. The requirements on \cancel{H}_T in the trigger and pre-selection reduce the peak near 0.5 substantially, but do not affect the tail above 0.55. In this tail, the simulation indicates a strong rejection of QCD multi-jet production. The distributions of $\cancel{H}_T/\cancel{E}_T$, $\min_j \Delta\phi_j^*$, and N_{jets} after all cuts are shown in Figure 3.4. It is apparent that these distributions alone would not clearly indicate the presence of a signal model such as LM6 in the data. However, the distributions of H_T typically differ substantially for signal models and the SM background, and the use of the H_T distribution of the selected events is discussed in

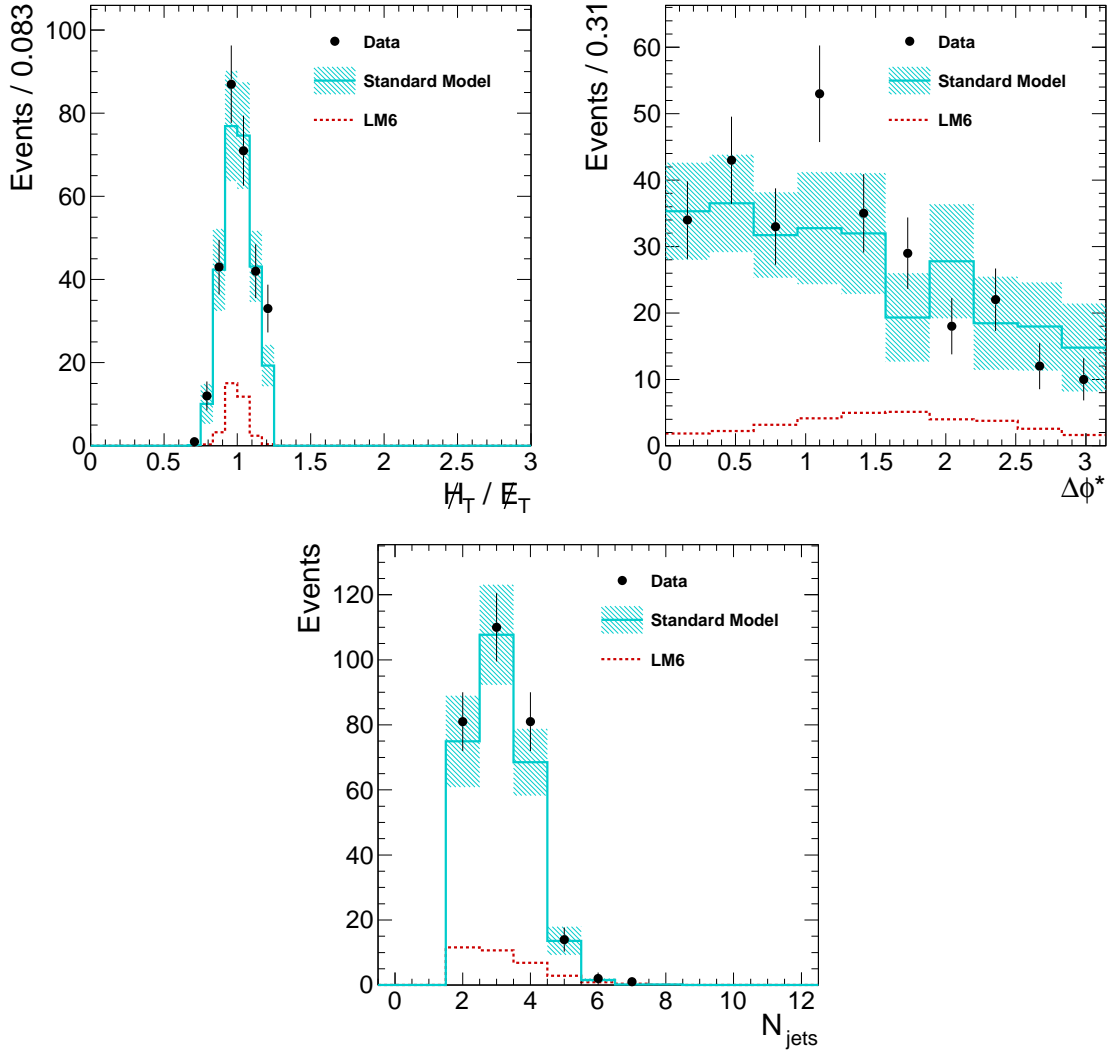


Figure 3.4: The observed distributions of H_T/\cancel{E}_T , the minimum $\Delta\phi^*$ of the selected jets, and the number of jets after all selection criteria. For illustration, SM expectations from the simulation are overlaid; the shaded band represents the uncertainty from finite MC statistics.

the following chapters.

Table 3.2: Yields obtained in the hadronic sample with $H_T > 375$ GeV. The MC entries are scaled to 1.1/fb. Standard Model is the sum of QCD, $t\bar{t}$, $Z + \text{jets}$, and $W \rightarrow l\nu + \text{jets}$; the $t\bar{t}$ column contains also single top production; the $Z + \text{jets}$ column includes both $Z \rightarrow \nu\bar{\nu} + \text{jets}$ and Drell-Yan di-lepton production. A trigger requirement is not applied to the MC samples; hence the yields are comparable to data only in the last two rows, at which point requirements stricter than the trigger have been applied.

Description	Data	Standard Model	QCD multi-jet	$t\bar{t}$	$Z + \text{jets}$	$W \rightarrow l\nu + \text{jets}$	LM1	LM6
input dataset	50970340	1.0304(5)e+9	9.867(5)e+8	2.514(2)e+5	9.348(5)e+6	3.4057(9)e+7	5.21(1)e+3	331(2)
trigger	14345008	-	-	-	-	-	-	-
BPTX coinc.	14320443	-	-	-	-	-	-	-
physics declared	14309673	-	-	-	-	-	-	-
good track frac. > 0.25	14309666	1.0304(5)e+9	9.867(5)e+8	2.514(2)e+5	9.348(5)e+6	3.4057(9)e+7	5.21(1)e+3	331(2)
HBHE noise filter	14181931	-	-	-	-	-	-	-
jet 1: $p_T > 100$ GeV	12546575	5.235(3)e+8	5.229(3)e+8	1.183(1)e+5	1.191(5)e+5	4.011(10)e+5	4.33(1)e+3	246(2)
jet 2: $p_T > 100$ GeV	6529962	1.902(2)e+8	1.900(2)e+8	5.065(9)e+4	1.64(2)e+4	6.53(4)e+4	3399(9)	202(2)
jet 1: $ \eta < 2.5$	6401921	1.812(1)e+8	1.811(1)e+8	4.988(9)e+4	1.60(2)e+4	6.37(4)e+4	3393(9)	202(2)
≥ 1 vertex	6401824	1.812(1)e+8	1.811(1)e+8	4.988(9)e+4	1.60(2)e+4	6.37(4)e+4	3393(9)	202(2)
muon veto	6388867	1.812(1)e+8	1.811(1)e+8	4.295(8)e+4	1.37(2)e+4	4.98(3)e+4	2978(8)	162(2)
electron veto	6371897	1.811(1)e+8	1.810(1)e+8	3.677(7)e+4	1.10(2)e+4	3.69(3)e+4	2623(8)	129(2)
photon veto	6343484	1.808(1)e+8	1.807(1)e+8	3.646(7)e+4	1.08(2)e+4	3.60(3)e+4	2590(8)	127(2)
“other” jet veto	5790603	1.781(1)e+8	1.780(1)e+8	3.550(7)e+4	1.06(2)e+4	3.52(3)e+4	2546(8)	126(1)
“other” muon veto	5427773	1.735(1)e+8	1.734(1)e+8	3.313(7)e+4	1.01(2)e+4	3.34(3)e+4	2239(7)	106(1)
$H_T > 375$ GeV	2170354	2.763(3)e+7	2.760(3)e+7	2.254(6)e+4	3.29(9)e+3	1.08(2)e+4	2076(7)	103(1)
$\cancel{H}_T/\cancel{E}_T < 1.25$	754345	1.462(2)e+7	1.460(2)e+7	1.098(4)e+4	2.32(8)e+3	7.7(1)e+3	1886(7)	98(1)
$\cancel{H}_T > 100$ GeV	90145	8.8(1)e+4	8.3(1)e+4	1.52(2)e+3	1.11(6)e+3	2.47(8)e+3	1743(6)	94(1)
$\Delta R > 0.3$ when $\Delta\phi^* < 0.5$	25605	2.27(7)e+4	1.99(7)e+4	8.1(1)e+2	7.0(5)e+2	1.29(5)e+3	1364(6)	75(1)
$\alpha_T > 0.55$	289	2.7(2)e+2	8(6)e-2	62(3)	1.2(2)e+2	9(1)e+1	538(4)	33(1)

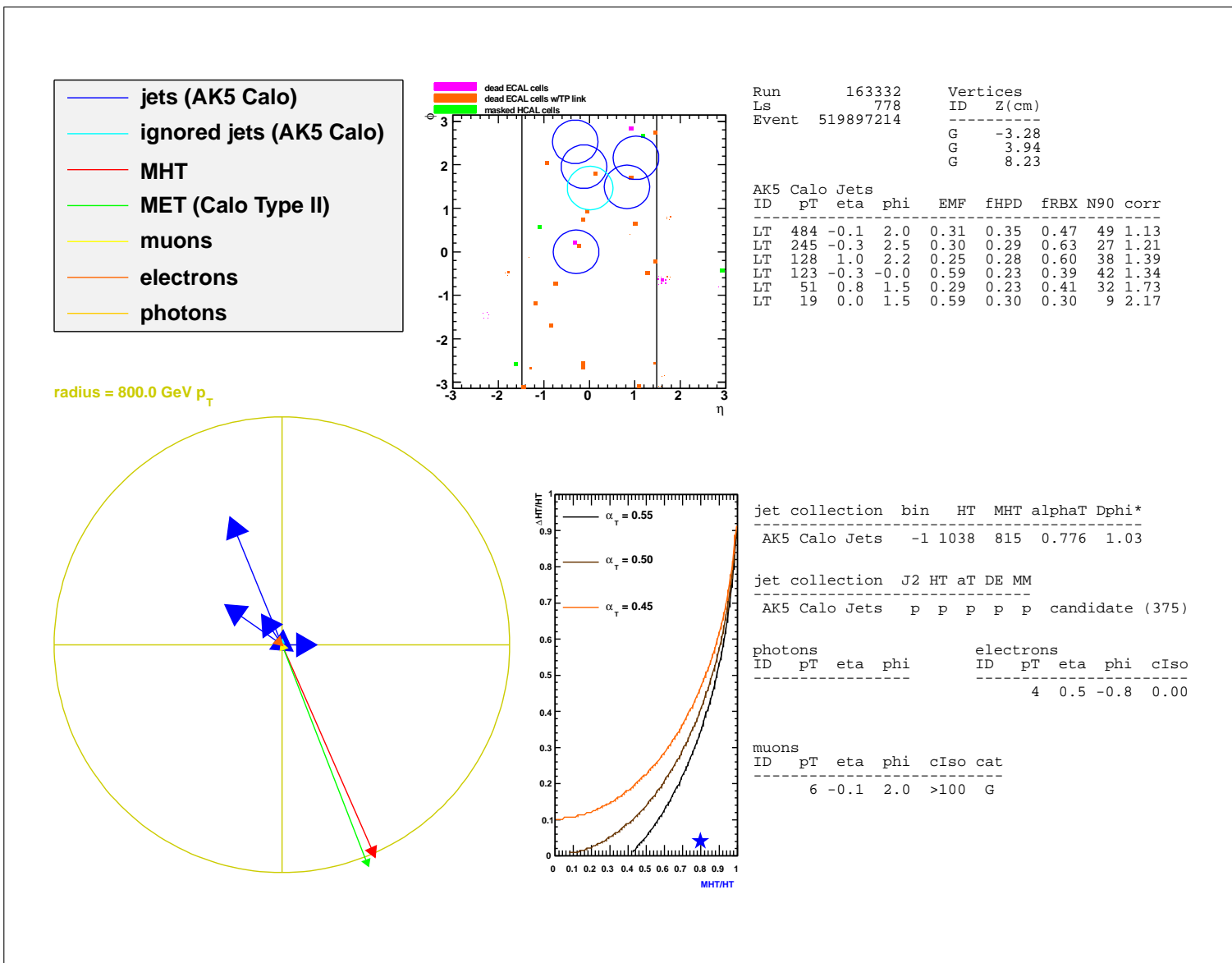


Figure 3.5: A reconstruction-level display of the highest H_T event in the hadronic sample.

Chapter 4

Background Constraints

The Standard Model production of $Z \rightarrow \nu\bar{\nu} + \text{jets}$, $W \rightarrow l\nu + \text{jets}$, and $t\bar{t}$ (“EWK” processes), can produce events with substantial missing transverse energy due to energetic escaping neutrinos when a Z or W (produced either directly or in a top quark decay) has a transverse boost. The yields from these processes are constrained using two control samples: one with events containing isolated photons, and one with events containing isolated muons. Simulated data is used to compute ratios of kinematically similar processes, which are used to connect the control samples to the signal sample. In addition, models of the candidate yield relative to the “bulk” event yield as functions of visible transverse energy are used both to allow for a potential contribution from multi-jet (“QCD”) events, and to provide an alternate view of the EWK background.

4.1 W + jets and top pair production

Events with a high- p_T W boson, produced either directly or in the decay of a top quark, form a background when the W decays to a neutrino (which escapes direct detection) and a lepton. The three main mechanisms are (a) an electron or muon can fall outside of the detector acceptance, or have p_T below the minimum considered;

(b) an electron or muon can fail the identification or isolation requirements used; or (c) a tau can decay hadronically. In these cases, which give approximately equal background contributions, the electron and muon vetoes are not effective.

A sample of $W + \text{jets}$ events is selected in which the W decays to a muon and neutrino, and in which the system of jets satisfies the search requirements. This sample is kinematically similar to the $W + \text{jets}$ background events; simulated events are used to connect the two. The muon sample selection was done by others, but is included here for completeness.

4.1.1 Selection of $W \rightarrow \mu\nu$ events

Events are collected with the same two-leg (H_T, \cancel{H}_T) triggers used for the hadronic signal sample, as muons typically deposit little energy in the calorimeters, and hence will only minimally perturb the set of jets used to compute H_T and \cancel{H}_T . All cuts on jet-based quantities are consistent with those applied in the hadronic search region. In addition, one muon is required with $p_T > 10$ GeV and $|\eta| < 2.4$, and satisfying the recommended “tight” identification requirements from [41]. *I.e.*, it must be identified as a global and tracker muon with χ^2/N_{dof} of the global muon fit < 10 ; at least one muon chamber hit must be used in the global fit which matches muon segments in at least two muon stations; the number of valid tracker hits must be ≥ 11 , including at least one pixel hit; the transverse impact parameter with respect to beam spot must be < 2 mm.

The muon is required to have $(\text{Iso}_{\text{TRK}} + \text{Iso}_{\text{ECAL}} + \text{Iso}_{\text{HCAL}})/p_T^\mu < 0.15$, where the Iso variables are the scalar sums of the transverse momenta of reconstructed tracks and the transverse energies measured in the electromagnetic and hadron calorimeters, within a cone of radius $\Delta R = 0.3$ in η, ϕ around the reconstructed muon direction. The track of the muon is excluded from the sum, as are calorimeter deposits occurring within a small “veto cone” around the extrapolated muon path.

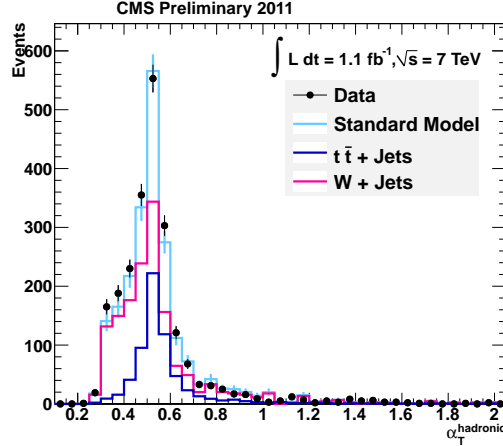


Figure 4.1: The distribution of α_T in the muon control sample. From [5].

Events with a second muon satisfying the above criteria are rejected, to eliminate any potential contribution from $Z \rightarrow \mu^+ \mu^-$. Events in which the muon matches a reconstructed jet, *i.e.* $\Delta R(\text{jet}, \text{muon}) < 0.5$, are rejected. Finally, the transverse mass of the W candidate, $m_T \equiv \sqrt{2p_T^\mu \cancel{E}_T (1 - \cos \Delta\phi(\mu, \cancel{E}_T))}$, is required to be at least 30 GeV.

The observed distributions of α_T is shown in Figure 4.1; the overlaid simulated data are generated with MadGraph. \cancel{H}_T , which estimates p_T^W , is required to be $> 0.4 \times H_T$, to increase the similarity with the final sample. The final requirement, $\alpha_T > 0.55$, supersedes this requirement.

4.1.2 Background estimation procedure

The yield of W+jet events in the hadronic selection $W_{\text{data}}^{\text{had}}$ is estimated using the event yield in the muon control sample, W_{data}^μ , and the ratio of the expected yields in these two samples, as determined with simulated samples:

$$W_{\text{data}}^{\text{had}} = W_{\text{data}}^\mu \times \frac{W_{\text{MC}}^{\text{had}}}{W_{\text{MC}}^\mu}. \quad (4.1)$$

In the final fit, the expected yield is used rather than the observed yield W_{data}^μ .

Table 4.1: Muon sample predictions for 1.1/fb. From [5].

H_T Bin (GeV)	275–325	325–375	375–475	475–575
MC W + $t\bar{t}$	$463.0 \pm 16.0_{\text{stat}}$	$171.2 \pm 9.5_{\text{stat}}$	$116.3 \pm 8.3_{\text{stat}}$	$43.7 \pm 5.1_{\text{stat}}$
MC μ + jets	$407.5 \pm 14.5_{\text{stat}}$	$179.1 \pm 9.6_{\text{stat}}$	$131.6 \pm 8.8_{\text{stat}}$	$48.7 \pm 5.5_{\text{stat}}$
MC Ratio	1.14	0.96	0.90	0.90
Data μ + jets	389	156	113	39
W + $t\bar{t}$ Pred.	442.0	149.1	101.9	35.2
	$\pm 22.4_{\text{stat}} \pm 132.6_{\text{syst}}$	$\pm 11.9_{\text{stat}} \pm 44.7_{\text{syst}}$	$\pm 9.6_{\text{stat}} \pm 30.6_{\text{syst}}$	$\pm 5.6_{\text{stat}} \pm 10.6_{\text{syst}}$
H_T Bin (GeV)	575–675	675–775	775–875	875– ∞
MC W + $t\bar{t}$	$17.5 \pm 3.2_{\text{stat}}$	$5.1 \pm 1.8_{\text{stat}}$	$1.1 \pm 0.7_{\text{stat}}$	$1.8 \pm 1.0_{\text{stat}}$
MC μ + jets	$13.3 \pm 2.9_{\text{stat}}$	$8.0 \pm 2.3_{\text{stat}}$	$3.2 \pm 1.4_{\text{stat}}$	$0.9 \pm 0.7_{\text{stat}}$
MC Ratio	0.90	0.90	0.90	0.90
Data μ + jets	17	5	0	0
W + $t\bar{t}$ Pred.	$15.3 \pm 3.7_{\text{stat}} \pm 4.6_{\text{syst}}$	$4.5 \pm 2.0_{\text{stat}} \pm 1.4_{\text{syst}}$	$0.0 \pm 1.0_{\text{stat}}$	$0.0 \pm 1.0_{\text{stat}}$

Nonetheless, the observed yield is used here for illustration, and the prediction is carried out in Table 4.1. Due to limited MC statistics, a fixed MC ratio is used for $H_T > 375$ GeV.

Contamination from QCD production of heavy flavor mesons and subsequent semi-leptonic decay was found to be negligible. The yields from single (anti)-top quark production and Drell-Yan di-lepton production are small and affect the ratio only negligibly. The fraction of fully-leptonic $t\bar{t}$ decays was found to be $\sim 5\%$, and the MC ratio was found not to change significantly when the relative fractions of W + jets and $t\bar{t}$ events were varied.

Systematic uncertainties

Following [65], the uncertainty on the muon acceptance times reconstruction and identification efficiency is quoted to be 6%. The probability of the lepton vetoes failing to veto a W decay is affected by uncertainty in tau-jet modeling (7%), lepton reconstruction inefficiency (100%), and the fraction of $t\bar{t} \rightarrow \tau\bar{\tau}$ decays (50%). These are propagated to the MC ratio, making the total uncertainty 30%.

4.2 Z + jets with invisible Z decay

Events in which a high- p_T Z^0 -boson is produced along with jets and decays to a pair of neutrinos form a significant background. To estimate the number of such events accepted by the search, events with a high- p_T photon are selected, the photon is ignored when computing the kinematic variables, and simulated data is used to connect the expected yield of photon + jet events to that of $Z \rightarrow \nu\bar{\nu}$ + jet events. The kinematics of the $Z \rightarrow \nu\bar{\nu}$ events and γ + jet events are expected to be similar, especially when the transverse momentum of the photon exceeds the Z^0 mass [66]. This method was first pursued in [67]. The simulated samples of QCD and γ + jets have been generated with MadGraph. Samples generated with PYTHIA were found to give similar results. Further, the contribution from W, Z, and $t\bar{t}$ processes, in which a decay electron could fake a photon, was found to be negligible.

4.2.1 Selection of photon + jet events

The events are collected using a single-photon trigger, with a p_T threshold of either 75 or 90 GeV, a calorimeter-based identification requirement, and depending upon the run range, loose isolation requirements. Candidate events are required to have exactly one photon with $p_T > 100$ GeV (at which threshold the trigger is found to be more than 98% efficient), satisfying the recommendations for isolated photon identification, as described in [68, 69] and reproduced in Table 4.2.

H/E represents the energy recorded in hits in the HCAL within a cone of $\Delta R = 0.15$ around the reconstructed photon, divided by the energy of the cluster of hits in the ECAL. σ_{inin} gives a measure of the width of the cluster in η , and is typically larger for a neutral pion decaying to two photons than for a single photon. Iso_{TRK} is defined as the scalar sum of the transverse momenta of the tracks within a cone of radius 0.4 around the reconstructed photon. Ignored are tracks within a cone of radius

Table 4.2: Variables and upper thresholds used for photon identification. From [68].

Variable	Requirement
ISO _{TRK}	$< 2.0 \text{ GeV} + 0.001 \times p_T$
ISO _{ECAL}	$< 4.2 \text{ GeV} + 0.006 \times p_T$
ISO _{HCAL}	$< 2.2 \text{ GeV} + 0.0025 \times p_T$
H/E	< 0.05
σ_{inin}	< 0.013

0.04, those having η within 0.015 of the photon, and those which do not originate within 0.1 cm of the beam-line; these exceptions avoid rejecting photons which convert within the tracker volume. ISO_{ECAL} represents the sum of the transverse energies of ECAL hits within $\Delta R = 0.4$ of the reconstructed photon, excluding those within $\Delta R = 0.06$ or within a strip $\Delta\eta = 0.04$ of the cluster center; ISO_{HCAL} represents the sum of the transverse energies of HCAL hits within $\Delta R = 0.4$, excluding those within $\Delta R = 0.15$. Further, a photon candidate is required not to match any set of hits in the pixel layers which is consistent with the track of an electron (or positron) producing the observed ECAL cluster. Both looser and stricter isolation requirements have been tested, and the net effect on the background prediction found to be small.

Spurious photon candidates, *i.e.* those whose most energetic hit occurs outside a plausible time window for collision products, or whose 4 nearest neighbors do not sum to at least 5% of the energy of the central hit, are rejected, as prescribed in [70]. Any second photon satisfying all requirements is required to have $p_T < 25 \text{ GeV}$.

Photons are required to be reconstructed within the barrel region of the ECAL ($|\eta^\gamma| < 1.45$), and to be separated from the nearest reconstructed jet ($\Delta R(\text{jet}, \text{photon}) > 1.0$). The hadronic (signal) selection is then applied, with variables, *e.g.* H_T and \cancel{H}_T , calculated from jets alone. The photon is ignored, as is any reconstructed “jet” within $\Delta R < 0.5$ of the photon, which includes the energy deposits out of which the photon has been reconstructed, and is redundant. Further, the photon p_T is added vectorially to the \cancel{E}_T in the $\cancel{H}_T/\cancel{E}_T$ cut, *i.e.* $\cancel{H}_T/|\cancel{E}_T + \vec{p}_T^\gamma|$, so that the cut has an effect analogous to its effect in the hadronic sample.

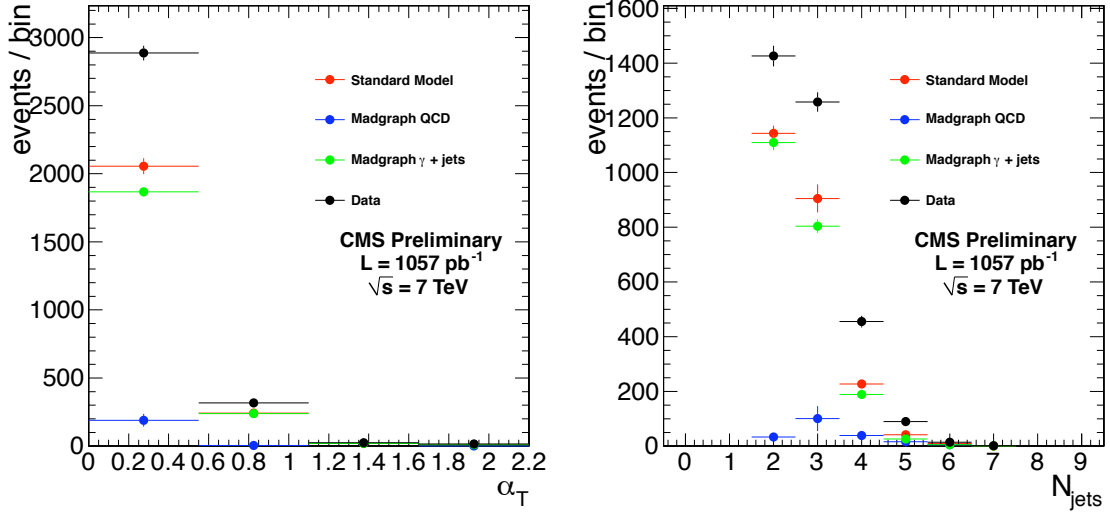


Figure 4.2: Distribution of α_T (left) and N_{jets} (right) for the photon sample before the cut on α_T . From [5].

The cut-flow is shown in Table 4.6. The data consist of the γ /Photon primary dataset. All samples, except for $Z \rightarrow \nu\bar{\nu}$, have been skimmed requiring at least one loosely identified photon with $p_T > 100$ GeV. The contribution from $t\bar{t}$, W, and $Z \rightarrow l^+l^-$ events was found to be negligible.

The distributions of α_T and N_{jets} are shown in Figure 4.2. The green histograms contain MadGraph photon + jet events; the blue histograms contain MadGraph QCD events, which contribute typically when a π^0 is reconstructed as an isolated photon. The photon typically recoils off a system of well-measured jets, as is visible in the left panel of Figure 4.3. The right panel indicates that, after all cuts, the trigger requirement for the photon has a small effect on the event yield.

4.2.2 Background estimation procedure

Simulated $Z \rightarrow \nu\bar{\nu} + \text{jets}$ events are selected as described above but dropping the photon requirement, as shown in Table 4.6. The predicted number of $Z \rightarrow \nu\bar{\nu}$ events in the hadronic signal region, $Z_{\text{data;inv}}^{\text{had}}$, is expressed as

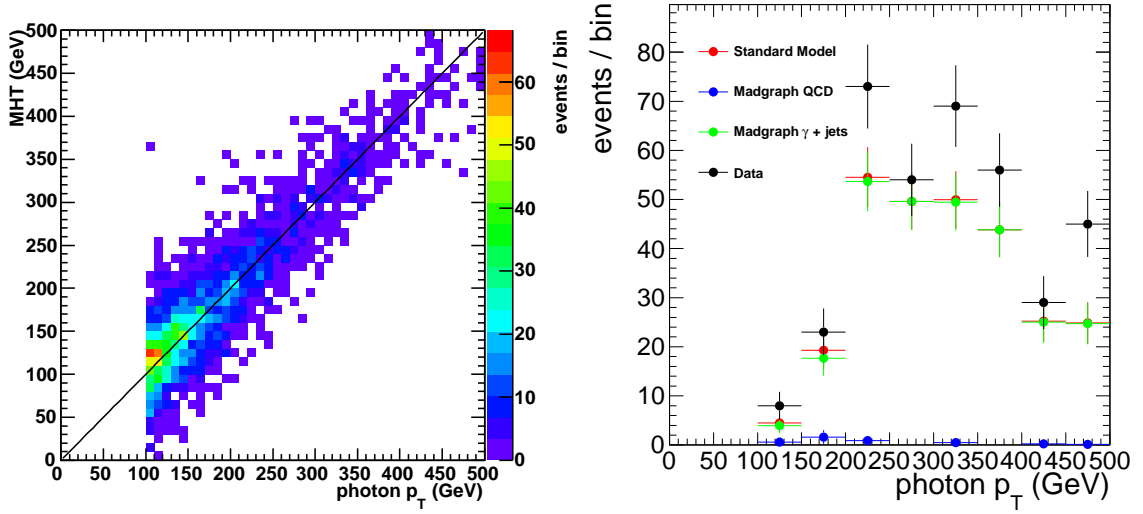


Figure 4.3: Left: The distribution (data) of $\#H_T$ vs. photon p_T before the α_T cut; the black line is $y = x$. Right: the distribution of photon p_T after the α_T cut; overflows are displayed in the last bin.

$$Z_{\text{data;inv}}^{\text{had}} = \frac{Z_{\text{MC}}^{\text{true}}}{\gamma_{\text{MC}}^{\text{true}}} \times \frac{P}{a_\gamma \times \epsilon_\gamma} \times \gamma_{\text{data}} \quad (4.2)$$

where:

- $Z_{\text{MC}}^{\text{true}}$ is the generator truth number of expected $Z \rightarrow \nu\bar{\nu}$ events in the hadronic signal sample.
- $\gamma_{\text{MC}}^{\text{true}}$ is the generator truth number of expected $\gamma + \text{jets}$ events in the photon control sample.
- P is the purity in MC of the sample ($\frac{\gamma+\text{jets}}{\text{all events}}$).
- $a \times \epsilon$ is the acceptance times efficiency for photons in MC for such events.
- γ_{data} is number of events in the photon control sample.

In the final fit, the expected yield is used rather than the observed yield γ_{data} . Nonetheless, the observed yield is used here for illustration, and the prediction is carried out in Table 4.3. Due to limited MC statistics, a fixed MC ratio and purity

Table 4.3: Photon sample predictions for 1.1/fb. From [5].

H_T Bin (GeV)	275–325	325–375	375–475	475–575
MC $Z \rightarrow \nu\bar{\nu}$	$212.6 \pm 20_{\text{stat}}$	$92.0 \pm 20_{\text{stat}}$	$61.3 \pm 20_{\text{stat}}$	$42.9 \pm 10_{\text{stat}}$
MC $\gamma + \text{jets}$	$613.1 \pm 20_{\text{stat}}$	$265.7 \pm 10_{\text{stat}}$	$168.6 \pm 10_{\text{stat}}$	$55.2 \pm 8.2_{\text{stat}}$
MC Ratio	0.35	0.35	0.44	0.44
Data $\gamma + \text{jets}$	867.5	313.7	214.6	68.5
Sample Purity	0.92	0.97	0.99	0.99
$Z \rightarrow \nu\bar{\nu}$ Prediction	276.8	105.3	93.5	29.8
	$\pm 9.5_{\text{stat}} \pm 110.7_{\text{syst}}$	$\pm 6.0_{\text{stat}} \pm 42.1_{\text{syst}}$	$\pm 6.4_{\text{stat}} \pm 37.4_{\text{syst}}$	$\pm 3.6_{\text{stat}} \pm 11.9_{\text{syst}}$
H_T Bin (GeV)	575–675	675–775	775–875	875– ∞
MC $Z \rightarrow \nu\bar{\nu}$	$5.1 \pm 5.1_{\text{stat}}$	$0.0 \pm 3.1_{\text{stat}}$	$3.1 \pm 3.1_{\text{stat}}$	$0.0 \pm 3.1_{\text{stat}}$
MC $\gamma + \text{jets}$	$23.5 \pm 5.1_{\text{stat}}$	$3.1 \pm 2.0_{\text{stat}}$	$3.1 \pm 2.0_{\text{stat}}$	$2.0 \pm 1.0_{\text{stat}}$
MC Ratio	0.44	0.44	0.44	0.44
Data $\gamma + \text{jets}$	24.5	12.3	4.1	4.1
Sample Purity	0.99	0.99	0.99	0.99
$Z \rightarrow \nu\bar{\nu}$ Prediction	10.7	5.3	1.8	1.8
	$\pm 2.2_{\text{stat}} \pm 4.3_{\text{syst}}$	$\pm 1.5_{\text{stat}} \pm 2.1_{\text{syst}}$	$\pm 0.9_{\text{stat}} \pm 0.7_{\text{syst}}$	$\pm 0.9_{\text{stat}} \pm 0.7_{\text{syst}}$

are used for $H_T > 375$ GeV. Yields have been scaled by 1.02 to account for the fact that the hadronic sample has 2% more integrated luminosity than the photon sample.

Systematic uncertainties

Because the ratio $Z_{\text{MC}}^{\text{true}}/\gamma_{\text{MC}}^{\text{true}}$ as well as the purity and photon acceptance are taken from the simulation, conservative uncertainties are assigned. A 30% theoretical uncertainty [66, 71] is assigned to the ratio $Z_{\text{MC}}^{\text{true}}/\gamma_{\text{MC}}^{\text{true}}$, taken from MadGraph. The identification criteria and variables are validated and agreement between data and simulation observed in [69]; however, given that these tests have been performed at lower H_T , an uncertainty of 20% is assigned for $a \times \epsilon$ and P . The theoretical and systematic uncertainties are added in quadrature, yielding a total systematic uncertainty of 40%.

4.2.3 Background cross-check: Estimation of $W \rightarrow \mu\nu + \text{jets}$ sample

To verify that the background estimation method for $Z \rightarrow \nu\bar{\nu}$ events performs as expected, and that the assigned systematic uncertainties are adequate, the $\gamma + \text{jets}$ sample is used to predict the number of $W \rightarrow \mu\nu$ events, which is kinematically

Table 4.4: Predictions of $W + \text{two jets}$ events using the photon sample for 1.1fb^{-1} . From [5].

H_T	$N_{\text{data}}^{\text{phot}}$	$N_{\text{MC}}^W/N_{\text{MC}}^{\text{phot}}$	$N_{\text{pred}W}^W$	N_{obs}^W
275	336	$0.42 \pm 0.04_{\text{MCstat}}$	$141.8 \pm 7.7_{\text{stat}} \pm 14.6_{\text{MCstat}} \pm 56.7_{\text{syst}}$	128
325	127	$0.42 \pm 0.04_{\text{MCstat}}$	$53.6 \pm 4.8_{\text{stat}} \pm 5.5_{\text{MCstat}} \pm 21.4_{\text{syst}}$	37
375	96	$0.42 \pm 0.04_{\text{MCstat}}$	$40.5 \pm 4.1_{\text{stat}} \pm 4.2_{\text{MCstat}} \pm 16.2_{\text{syst}}$	36
475	27	$0.42 \pm 0.04_{\text{MCstat}}$	$11.4 \pm 2.2_{\text{stat}} \pm 1.2_{\text{MCstat}} \pm 4.6_{\text{syst}}$	12
575	13	$0.42 \pm 0.04_{\text{MCstat}}$	$5.5 \pm 1.5_{\text{stat}} \pm 0.6_{\text{MCstat}} \pm 2.2_{\text{syst}}$	2

similar to the process $Z \rightarrow \nu\bar{\nu} + \text{jets}$. To reject events originating from $t\bar{t}$ production, and to obtain a pure $W + \text{jets}$ sample, the number of jets is limited to two. The number of W events is then estimated as follows:

$$N_{\text{data}}^W = N_{\text{data}}^{\text{phot}} \times \frac{N_{\text{MC}}^W}{N_{\text{MC}}^{\text{phot}}}. \quad (4.3)$$

The factor $N_{\text{MC}}^W/N_{\text{MC}}^{\text{phot}}$, which includes selection efficiencies and acceptance, is taken from MC simulation. Within the statistical precision of the MC samples, it is found to be approximately independent of H_T ; thus, a constant factor of 0.42 ± 0.04 is used. The results are summarized in Table 4.4. The predicted numbers of muon events are seen to agree well with the observed numbers within the assigned systematic uncertainties.

4.3 Tail fraction dependence upon visible transverse energy

Signal models in which two heavy particles are produced, *e.g.* squark-squark or squark-gluino, and in which each particle decays to one or two quarks and an escaping neutral particle, will have a (broad) peak in H_T , whose location is determined by the masses of the parent and daughter particles. Two examples are shown in Figure 3.1.

The process $t\bar{t} \rightarrow Wb\bar{W}\bar{b}$ is similar. In the rest frame of a top [14],

$$E_b = \frac{m_t^2 - m_W^2 + m_b^2}{2m_t} . \quad (4.4)$$

For background $t\bar{t}$ events, typically one W decays hadronically and the other is “invisible” to the search, having a low- p_T or non-identified lepton. Thus for a top pair produced on threshold, the visible transverse energy is some fraction of m_t plus some fraction of E_b , or approximately 100–200 GeV, beyond which the H_T distribution falls.

The distributions of H_T for $Z \rightarrow \nu\bar{\nu} + \text{jets}$ and $W + \text{jets}$ events fall as well. A quantity that captures this difference—a mass scale apparent for a signal model, compared with the falling background distribution—is

$$R_{\alpha_T} = \frac{N_{\alpha_T > 0.55}}{N_{\alpha_T < 0.55}} , \quad (4.5)$$

where $N_{\alpha_T > 0.55}$ represents the final event yield in a bin of H_T , and $N_{\alpha_T < 0.55}$ represents the event yield after pre-selection, but failing the α_T cut, in the same bin of H_T . As the denominator is intended to represent a “bulk” event yield, triggers based solely on H_T are used to collect the events, and no \cancel{H}_T , $\cancel{H}_T/\cancel{E}_T$, nor “dead”-ECAL-region cut is applied.

The shape of this ratio for simulated SM events, with two example signal models stacked on top, is shown in the left plot of Figure 4.4. The signals show broad “peaks” on top of the flat SM-only ratio. The final bin is inclusive (*i.e.* > 875 GeV), and the error bars represent statistical error due to finite simulated event samples. The observed values of R_{α_T} are listed in Table 4.5 and shown in Figure 4.5.

4.3.1 EWK

$R_{\alpha_T}^{\text{EWK}}$, *i.e.* the background yield from SM processes with vector bosons divided by the “bulk” event yield, is modeled as constant vs. H_T . The p -value for a constant fit to

Table 4.5: The event yields used in the numerator and denominator of R_{α_T} and the resulting values, in bins of H_T , for 1.1 fb^{-1} . In the lowest bin, R_{α_T} has been multiplied by 1.01 to account for trigger inefficiency. Also shown are the mean values of H_T computed from the events with $\alpha_T < 0.55$. From [5].

H_T Bin (GeV)	275–325	325–375	375–475	475–575
$\alpha_T > 0.55$	782	321	196	62
$\alpha_T < 0.55$	$5.73 \cdot 10^7$	$2.36 \cdot 10^7$	$1.62 \cdot 10^7$	$5.12 \cdot 10^6$
$R_{\alpha_T} (10^{-5})$	$1.38 \pm 0.05_{\text{stat}}$	$1.36 \pm 0.08_{\text{stat}}$	$1.21 \pm 0.09_{\text{stat}}$	$1.21 \pm 0.15_{\text{stat}}$
$\langle H_T \rangle$ (GeV)	296	346	413	514
H_T Bin (GeV)	575–675	675–775	775–875	875– ∞
$\alpha_T > 0.55$	21	6	3	1
$\alpha_T < 0.55$	$1.78 \cdot 10^6$	$6.89 \cdot 10^5$	$2.90 \cdot 10^5$	$2.60 \cdot 10^5$
$R_{\alpha_T} (10^{-5})$	$1.18 \pm 0.26_{\text{stat}}$	$0.87 \pm 0.36_{\text{stat}}$	$1.03 \pm 0.60_{\text{stat}}$	$0.39 \pm 0.52_{\text{stat}}$
$\langle H_T \rangle$ (GeV)	616	717	818	919

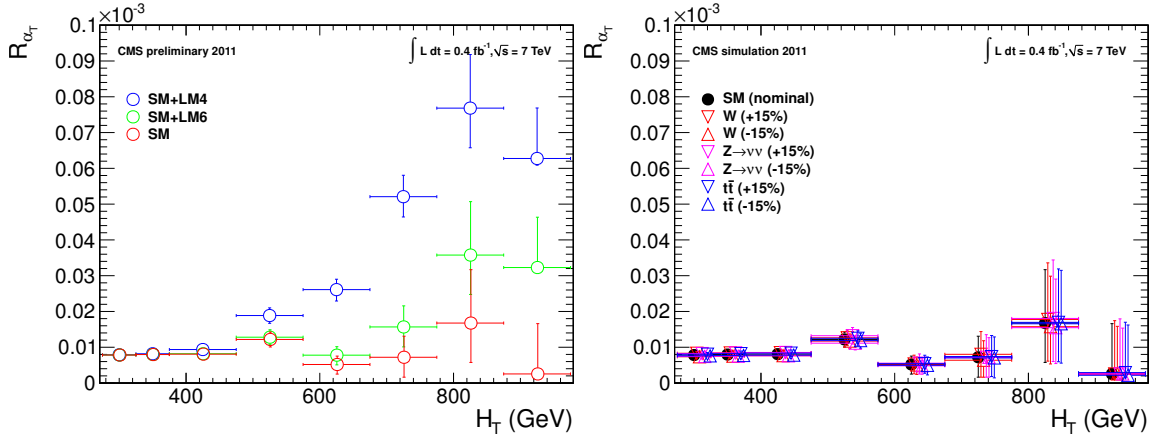


Figure 4.4: Left: the dependence of R_{α_T} on H_T from simulated events. Right: the same dependence, when the cross sections of the EWK background components are individually varied by $\pm 15\%$. The markers are artificially offset for clarity. Modified from [5].

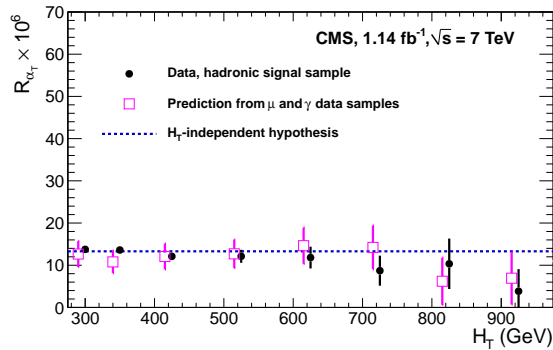


Figure 4.5: The observed dependence of R_{α_T} on H_T , as well as the prediction from the control samples for the total EWK background. The markers are artificially offset for clarity. Modified from [2].

the simulated ratio gives 0.50. The cross sections of the sub-components were varied individually by $\pm 15\%$, reflecting current knowledge of the cross sections [72, 73], and a fit to a constant was performed for each of the variations. The minimum p -value obtained was > 0.4 , indicating compatibility with the hypothesis. The results are shown in the right plot of Figure 4.4. Variations obtained by modifying the cross sections by $\pm 50\%$ were also found to be compatible.

The muon and photon control samples provide an additional test of the shape of $R_{\alpha_T}^{\text{EWK}}$: the background predictions illustrated in the previous two sections are summed to estimate the yields of EWK background vs. H_T , which are then divided by the observed “bulk” yields. The result is shown in Figure 4.5; the predicted ratio is consistent with flat within systematic uncertainties. Also shown is the result of a simultaneous fit to the muon, photon, and hadronic samples assuming the presence of SM EWK processes only. It is explained in detail in Section 6.1.

4.3.2 QCD

$R_{\alpha_T}^{\text{QCD}}$, *i.e.* the SM background yield from multi-jet events divided by the “bulk” event yield, is modeled as a falling exponential, as described in detail in Section 5.1.2. By design, the background from multi-jet events is expected to be negligible, and so two

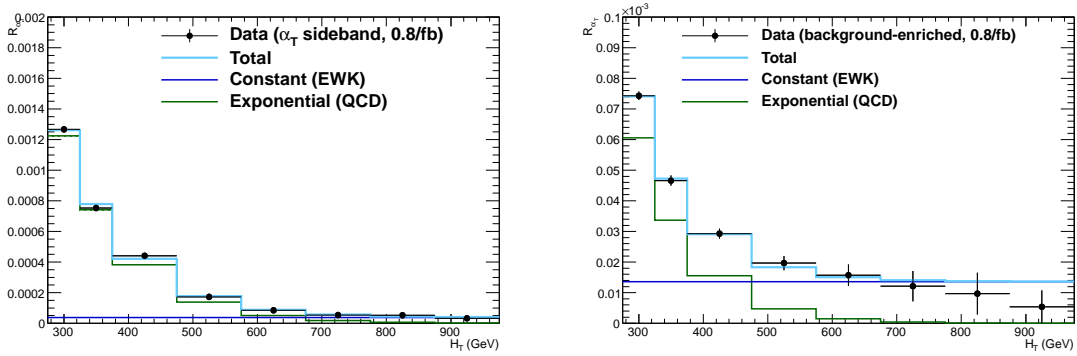


Figure 4.6: R_{α_T} vs. H_T observed in 770/pb of data for the α_T sideband sample (left) and the background-enriched sample (right). Also shown are the results of fits using the functional forms described in the text.

samples designed to enhance QCD background are used to validate the form of $R_{\alpha_T}^{\text{QCD}}$ assumed. Only the first 770/pb of data are used, in which sample the predominant \cancel{H}_T requirement in the trigger (70 GeV) was still low enough to collect these samples efficiently.

The first sample is the “ α_T sideband” of events passing all cuts, except requiring $0.52 < \alpha_T < 0.55$ rather than $0.55 < \alpha_T$. The sample is chosen to admit some QCD events in which a jet either (a) contains an energetic neutrino, or (b) is moderately mis-measured. It also admits some EWK events with vector bosons with lower p_T than those found in the signal sample. These yields are then divided by the bulk yields, and the result is shown in the left plot of Figure 4.6.

For the second sample, $0.55 < \alpha_T$ is required, but the $\cancel{H}_T/\cancel{E}_T$ and “dead”-ECAL-region cuts are removed. It is chosen to admit some QCD events in which either (a) a jet is severely mis-measured, and falls below the p_T threshold used to select jets, or (b) multiple low- p_T jets aligned in azimuthal angle fail to be considered. The resulting ratio is shown in the right plot of Figure 4.6.

In both samples, which admit different classes of QCD events, a constant component plus a falling exponential component provides a satisfactory description of R_{α_T} vs. H_T . The value of the constant component in the second sample agrees with that

predicted by the direct EWK background estimates as well as that resulting from the simultaneous fit to the muon, photon, and hadronic (signal) samples, both shown in Figure 4.5.

Table 4.6: Yields obtained in the photon control sample with $H_T > 375$ GeV. The MC entries are scaled to 1.1/fb. MC total is the sum of QCD and $\gamma + \text{jets}$. Comparison of data and MC is possible after the horizontal line, when the applied cuts are stricter than the skim criteria used to obtain the input datasets (see text). A hyphen indicates that a given cut was not applied to a particular sample. The cuts that are not photon-specific are explained in Sections 3.2 and 3.3.

Description	Data	$Z \rightarrow \nu\bar{\nu}$	MC total	QCD	$\gamma + \text{jets}$
input dataset	429994	6.041(4)e+6	3.30(7)e+5	1.00(7)e+5	2.299(10)e+5
BPTX coinc.	428259	-	-	-	-
physics declared	427974	-	-	-	-
≤ 10 tracks or > 0.25 good frac.	427972	6.041(4)e+6	3.30(7)e+5	1.00(7)e+5	2.299(10)e+5
HBHE noise filter	427826	-	-	-	-
trigger	420433	-	-	-	-
≥ 1 vertex	420124	6.032(4)e+6	3.30(7)e+5	1.00(7)e+5	2.299(10)e+5
jet 1: $p_T > 100$ GeV	265942	6.77(4)e+4	2.38(6)e+5	7.6(6)e+4	1.628(8)e+5
jet 2: $p_T > 100$ GeV	42314	6.9(1)e+3	3.9(2)e+4	2.1(2)e+4	1.85(2)e+4
jet 1: $ \eta < 2.5$	41518	6.8(1)e+3	3.3(1)e+4	1.5(1)e+4	1.83(2)e+4
$H_T > 375$ GeV	12558	2.27(8)e+3	1.16(4)e+4	4.4(4)e+3	7.24(9)e+3
$p_T^\gamma > 100$ GeV	6966	-	5.53(8)e+3	9.7(6)e+2	4.56(6)e+3
$ \eta^\gamma < 1.4$	4921	-	3.89(7)e+3	6.1(5)e+2	3.29(5)e+3
$\Delta R(\text{photon, jet}) > 1.0$	3650	-	2.52(6)e+3	2.1(5)e+2	2.31(4)e+3
photon 2: $p_T < 25$ GeV	3635	-	2.52(6)e+3	2.1(5)e+2	2.31(4)e+3
photon veto	-	2.27(8)e+3	-	-	-
“other” jet veto	3602	2.24(8)e+3	2.50(6)e+3	2.1(5)e+2	2.30(4)e+3
electron veto	3563	2.24(8)e+3	2.48(6)e+3	2.0(5)e+2	2.28(4)e+3
muon veto	3555	2.24(8)e+3	2.48(6)e+3	2.0(5)e+2	2.28(4)e+3
“other” muon veto	3244	2.08(8)e+3	2.33(6)e+3	1.9(5)e+2	2.13(4)e+3
$\alpha_T > 0.55$	357	1.4(2)e+2	2.7(1)e+2	4(2)	2.7(1)e+2
$\cancel{E}_T/\cancel{p}_T < 1.25$	-	1.2(2)e+2	-	-	-
$\cancel{E}_T/ \cancel{E}_T + \vec{p}_T^\gamma < 1.25$	336	-	2.5(1)e+2	1.9(10)	2.5(1)e+2
$\Delta R(\text{jet, dead region}) > 0.3$ when $\Delta\phi^* < 0.5$	321	1.1(2)e+2	2.5(1)e+2	1.9(10)	2.4(1)e+2

Chapter 5

Statistical Framework

The likelihood model used to interpret the observations in the signal and control samples is described in Section 5.1, and the method used to set limits on the cross sections of signal models is described in Section 5.2.

5.1 Likelihood model

5.1.1 Hadronic sample

Let N be the number of bins of H_T , which need not have equal width. Let n^i represent the number of events observed satisfying all selection requirements in each H_T bin i . Then the likelihood of the observations is written this way:

$$L_{hadronic} = \prod_i \text{Pois}(n^i | b^i + s^i) \quad (5.1)$$

where b^i represents the expected Standard Model background in bin i , s^i represents the expected number of signal events in bin i , and Pois represents the Poisson distribution. It is assumed that $b^i \equiv \text{EWK}^i + \text{QCD}^i$, where EWK^i is the expected yield of electroweak events in bin i , and QCD^i is the expected yield of QCD events in bin i .

5.1.2 H_T evolution model

The hypothesis that for a process p the α_T ratio falls exponentially in H_T can be written this way:

$$R_{\alpha_T}(H_T) = Ae^{-kH_T} \quad (5.2)$$

where A and k are parameters whose values will be determined. A constant ratio is equivalent to requiring $k = 0$. Let m_i represent the number of events observed with $\alpha_T \leq 0.55$ in each H_T bin i , as discussed in Section 4.3, and let $\langle H_T \rangle^i$ represent the mean H_T of such events. The expected background from the process is written thus:

$$b_p^i = \int_{x_i}^{x_{i+1}} \frac{dN}{dH_T} R_{\alpha_T} dH_T \quad , \quad (5.3)$$

where $\frac{dN}{dH_T}$ is the distribution of H_T for events with $\alpha_T \leq 0.55$, x_i is the lower edge of the bin, and x_{i+1} is the upper edge of the bin (∞ for the final bin). It is assumed that

$$\frac{dN}{dH_T}(x) = \sum_i m^i \delta(x - \langle H_T \rangle^i) \quad , \quad (5.4)$$

i.e. within a bin the whole distribution occurs at the mean value of H_T in that bin.

Then

$$b_p^i = \int_{x_i}^{x_{i+1}} m^i \delta(x - \langle H_T \rangle^i) A e^{-kx} dx = m^i A e^{-k\langle H_T \rangle^i} \quad , \quad (5.5)$$

and in particular,

$$\begin{aligned} \text{EWK}^i &= m^i A_{\text{EWK}} \\ \text{QCD}^i &= m^i A_{\text{QCD}} e^{-k_{\text{QCD}} \langle H_T \rangle^i} \quad . \end{aligned} \quad (5.6)$$

5.1.3 Electroweak control samples

Let $Z_{inv}^i \equiv f_{Z_{inv}}^i \times \text{EWK}^i$, and $ttW^i \equiv (1 - f_{Z_{inv}}^i) \times \text{EWK}^i$. Each $f_{Z_{inv}}^i$ is a fit parameter, and represents the fraction of the expected EWK background in bin i which is from $Z \rightarrow \nu\bar{\nu}$ events. Thus the variable Z_{inv}^i represents the expected number

of $Z \rightarrow \nu\bar{\nu}$ events in H_T bin i of the hadronically selected sample, and the variable ttW^i represents the expected number of events from SM W -boson production (including top quark decays) in H_T bin i of the hadronically selected sample.

In each bin of H_T , there are two measurements: n_{ph} , and n_{mu} , representing the event counts in the photon and muon control samples. As discussed in Sections 4.1.2 and 4.2.2, each of these measurements has a corresponding yield in simulated data: MC_{ph} and MC_{mu} . The simulation also gives expected amounts of Z_{inv} and $t\bar{t} + W$ in the hadronically-selected sample: $MC_{Z_{inv}}$ and $MC_{t\bar{t}+W}$. Let i label the H_T bin, let σ_{phZ}^{inp} and σ_{muW}^{inp} represent the relative systematic uncertainties for the control sample constraints. After defining

$$r_{ph}^i = \frac{MC_{ph}^i}{MC_{Z_{inv}}^i}; r_{mu}^i = \frac{MC_{mu}^i}{MC_{t\bar{t}+W}^i} \quad , \quad (5.7)$$

these likelihood functions are used:

$$L_{ph} = \text{Gaus}(1.0 | \rho_{phZ}, \sigma_{phZ}^{inp}) \times \prod_i \text{Pois}(n_{ph}^i | \rho_{phZ} r_{ph}^i Z_{inv}^i) \quad (5.8)$$

$$L_{mu} = \text{Gaus}(1.0 | \rho_{muW}, \sigma_{muW}^{inp}) \times \prod_i \text{Pois}(n_{mu}^i | \rho_{muW} r_{mu}^i ttW^i + s_{mu}^i) \quad . \quad (5.9)$$

The parameters ρ_{phZ} and ρ_{muW} represent ‘‘correction factors’’ that accommodate the systematic uncertainties associated with the control-sample-based background constraints. Each is treated as fully correlated among the H_T bins.

5.1.4 Contributions from signal

Let x represent the cross section for a particular signal model, and let l represent the recorded luminosity. Let ϵ_{had}^i (resp. ϵ_{μ}^i) be the analysis efficiency as simulated for the model in H_T bin i of the hadronic (resp. muon control) sample. Let δ represent the relative uncertainty on the signal yield, assumed to be fully correlated among the bins,

and let ρ_{sig} represent the “correction factor” to the signal yield which accommodates this uncertainty. Let f represent an unknown multiplicative factor on the signal cross section, for which an allowed interval shall be determined.

Then the expected hadronic signal yield s^i from Equation 5.1 is written as $s^i \equiv f\rho_{sig}xl\epsilon_{had}^i$, and the “signal contamination” in the muon control sample s_{mu}^i from Equation 5.9 is treated analogously: $s_{mu}^i \equiv f\rho_{sig}xl\epsilon_{mu}^i$. The systematic uncertainty on the signal efficiency is included via an additional term in the likelihood:

$$L_{sig} = \text{Gaus}(1.0|\rho_{sig}, \delta) \quad . \quad (5.10)$$

5.1.5 Total likelihood

The likelihood function used is the product of the likelihood functions described in the previous sections:

$$L = L_{hadronic} \times L_{mu} \times L_{ph} \times L_{sig} \quad (5.11)$$

In addition to the parameter of interest f , there are $6 + N$ nuisance parameters: $A_{\text{QCD}}, k_{\text{QCD}}, A_{\text{EWK}}, \{f_{Zinv}^i\}$, as well as the “systematic” variables $\rho_{phZ}, \rho_{muW}, \rho_{sig}$.

5.2 Limits

The CL_s method [74] is used to test signal models. The test statistic chosen to rank experiments from least to most signal-like is specified in [75]:

$$q_\mu = \begin{cases} -2 \log \lambda(\mu) & \text{when } \mu \geq \hat{\mu} \\ 0 & \text{otherwise} \end{cases} \quad . \quad (5.12)$$

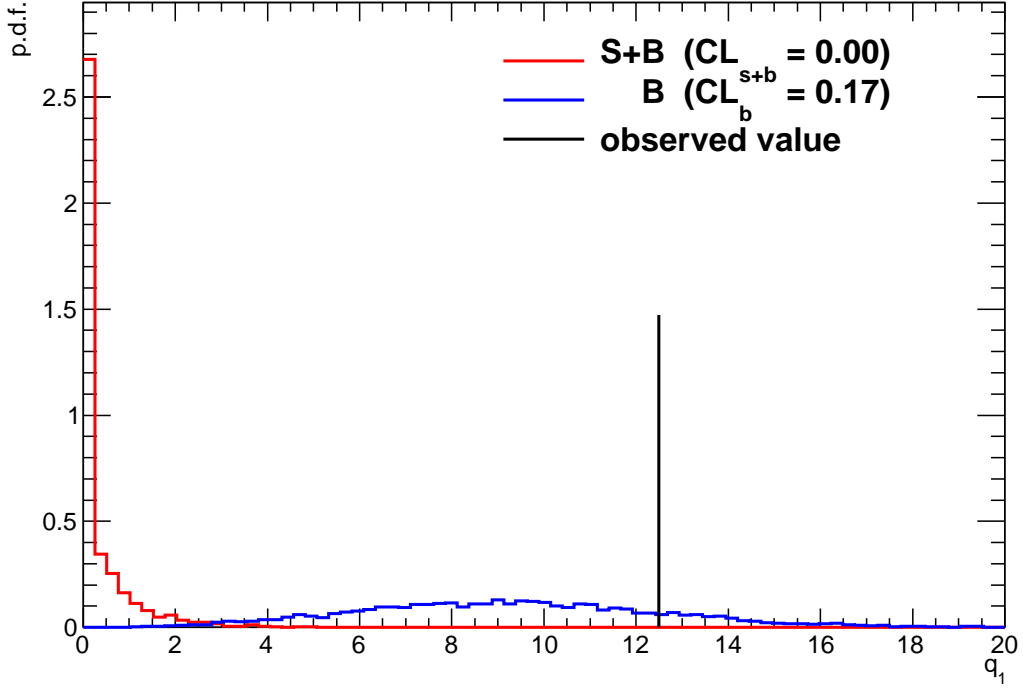


Figure 5.1: The distributions of the test statistic for the example model LM6 under the two hypotheses; also shown is the observed value.

Here

$$\lambda(\mu) = \frac{L(\mu, \theta_\mu)}{L(\hat{\mu}, \hat{\theta})} \quad (5.13)$$

is the profile likelihood ratio, in which $\mu \equiv f$ from Section 5.1.4, is the parameter characterizing the signal strength, with $\mu > 0$; $\hat{\mu}$ is its maximum likelihood (ML) value; $\hat{\theta}$ is the set of ML values of the nuisance parameters; θ_μ is the set of (conditional) ML values of the nuisance parameters for a given value of μ .

When $\mu \equiv f = 1$, the signal model is considered at its nominal cross section. For the example model LM6, the distributions of q_1 over pseudo-experiments from the SM-only and LM6+SM hypotheses are shown in Figure 5.1, along with the value of the q_1 observed in data. CL_b and CL_{s+b} are defined as one minus the quantiles of the observed value in the two distributions, and $CL_s \equiv CL_{s+b}/CL_b$. A model is considered to be excluded at 95% confidence level when $CL_s \leq 0.05$.

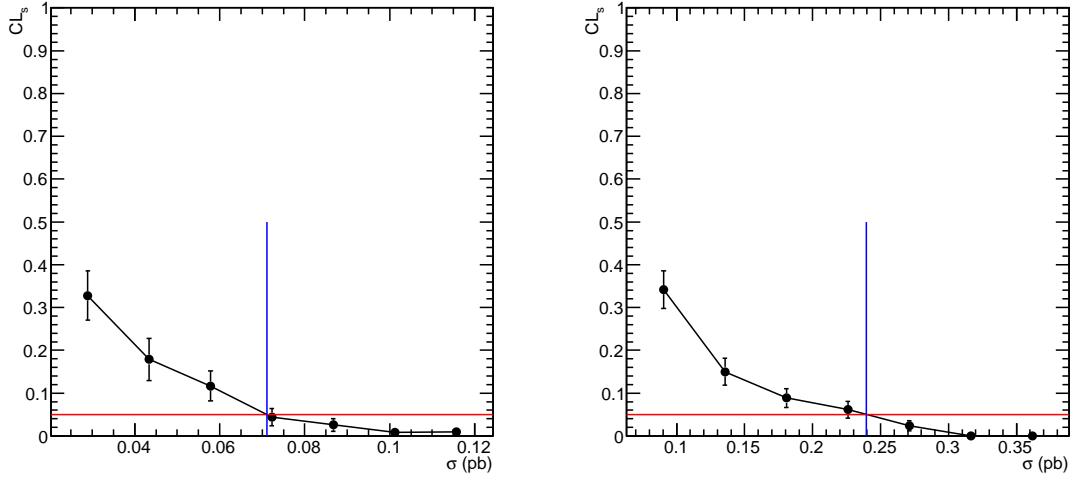


Figure 5.2: CL_s vs. $f[\times 1 \text{ pb}]$ for two different signal models, in this case pairs of $(m_{\text{gluino}}, m_{\text{LSP}})$ within the simplified model T1. The blue line segments indicate where the interpolated curves cross 0.05, *i.e.* the upper limits for the models' cross sections.

An alternative to binary exclusion is to place an upper limit on the cross section of a given model, *i.e.* determine the value of f at which $CL_s = 0.05$. To do so, an approximate value is found using the shape of the profile likelihood ratio as a function of f . CL_s is then computed at nearby values of f , and the upper limit is determined using linear interpolation. Two examples of this procedure are shown in Figure 5.2.

Chapter 6

Results and Interpretation

The results of the search consist of the observed yields in the hadronic signal sample and the muon and photon control samples, collected in Table 6.1, along with the “bulk” hadronic yields, photon-to-Z ratio, and W muon-to-hadronic ratio from Chapter 4. The likelihood model specified in Section 5.1 is used to relate these observations to each other, accommodate systematic uncertainty, and account for the possible presence of signal. The compatibility of the Standard Model, and of each of a variety of signal models is tested below.

6.1 Standard Model

Contributions to the likelihood from signal are dropped, and the likelihood function is maximized over all parameters using RooFit [76] and MINUIT [77]. The resulting yields are listed in Table 6.1 and displayed in Figure 6.1. Goodness-of-fit is determined using a method from [78]. The value L_{\max}^{data} of the likelihood function at its maximum is noted. The likelihood function (using the ML parameter values) is then used as a p.d.f. for the observations to generate many pseudo-experiments. For each pseudo-experiment, the likelihood function is again maximized over all parameters, and the value L_{\max} entered in a histogram. The quantile of L_{\max}^{data} in this histogram is

Table 6.1: Comparison of the observed yields in the different H_T bins of the hadronic, $\mu + \text{jets}$, and $\gamma + \text{jets}$ samples with the expectations and uncertainties given by the simultaneous fit to the SM-only hypothesis. From [2].

H_T bin (GeV)	275–325	325–375	375–475	475–575	575–675	675–775	775–875	>875
SM hadronic	787^{+32}_{-22}	310^{+8}_{-12}	202^{+9}_{-9}	$60.4^{+4.2}_{-3.0}$	$20.3^{+1.8}_{-1.1}$	$7.7^{+0.8}_{-0.5}$	$3.2^{+0.4}_{-0.2}$	$2.8^{+0.4}_{-0.2}$
Data hadronic	782	321	196	62	21	6	3	1
SM $\mu + \text{jets}$	367^{+15}_{-15}	182^{+8}_{-9}	113^{+8}_{-7}	$36.5^{+3.8}_{-3.3}$	$13.4^{+2.2}_{-1.8}$	$4.0^{+1.4}_{-1.2}$	$0.8^{+0.9}_{-0.1}$	$0.7^{+0.9}_{-0.1}$
Data $\mu + \text{jets}$	389	156	113	39	17	5	0	0
SM $\gamma + \text{jets}$	834^{+28}_{-30}	325^{+17}_{-17}	210^{+12}_{-12}	$64.7^{+6.9}_{-7.0}$	$21.1^{+3.9}_{-4.3}$	$10.5^{+2.5}_{-2.6}$	$6.1^{+0.9}_{-1.7}$	$5.5^{+0.9}_{-1.6}$
Data $\gamma + \text{jets}$	849	307	210	67	24	12	4	4

interpreted as a p -value. The value obtained is 0.56.

The uncertainties on the fit yields listed in Table 6.1 are determined in a similar fashion. For each pseudo-experiment, the fit yields for each bin of each sample are entered into separate histograms. The 16% and 84% quantiles of these histograms are found, and their differences from the ML values are reported as uncertainties.

The maximum-likelihood parameter values are given in Table 6.2, and their correlation matrix is shown in Figure 6.2. Limits are placed on the parameters `fZinv` to avoid obtaining a best-fit estimate of exactly zero events in bins containing zero observed events. Not doing so would have prevented the observation of any events in such bins in the generated pseudo-experiments. The results of an alternate approach in which `fZinv` is modeled as linear with H_T , and limited only within the physical range $[0, 1]$, are compatible with the nominal results, as shown in Figure 6.3.

The observed and best-fit yields are displayed again in Figure 6.4, divided in each H_T bin by the observed number of “bulk” events, as discussed in Section 4.3. The functional forms used to describe the different background components—a ratio independent of H_T for the EWK background, and an exponentially falling ratio for potential QCD background—are apparent. As a test, the exponentially falling component is fixed to zero and the data refit. The resulting p -value from the simultaneous fit is 0.41, indicating compatibility with this model as well.

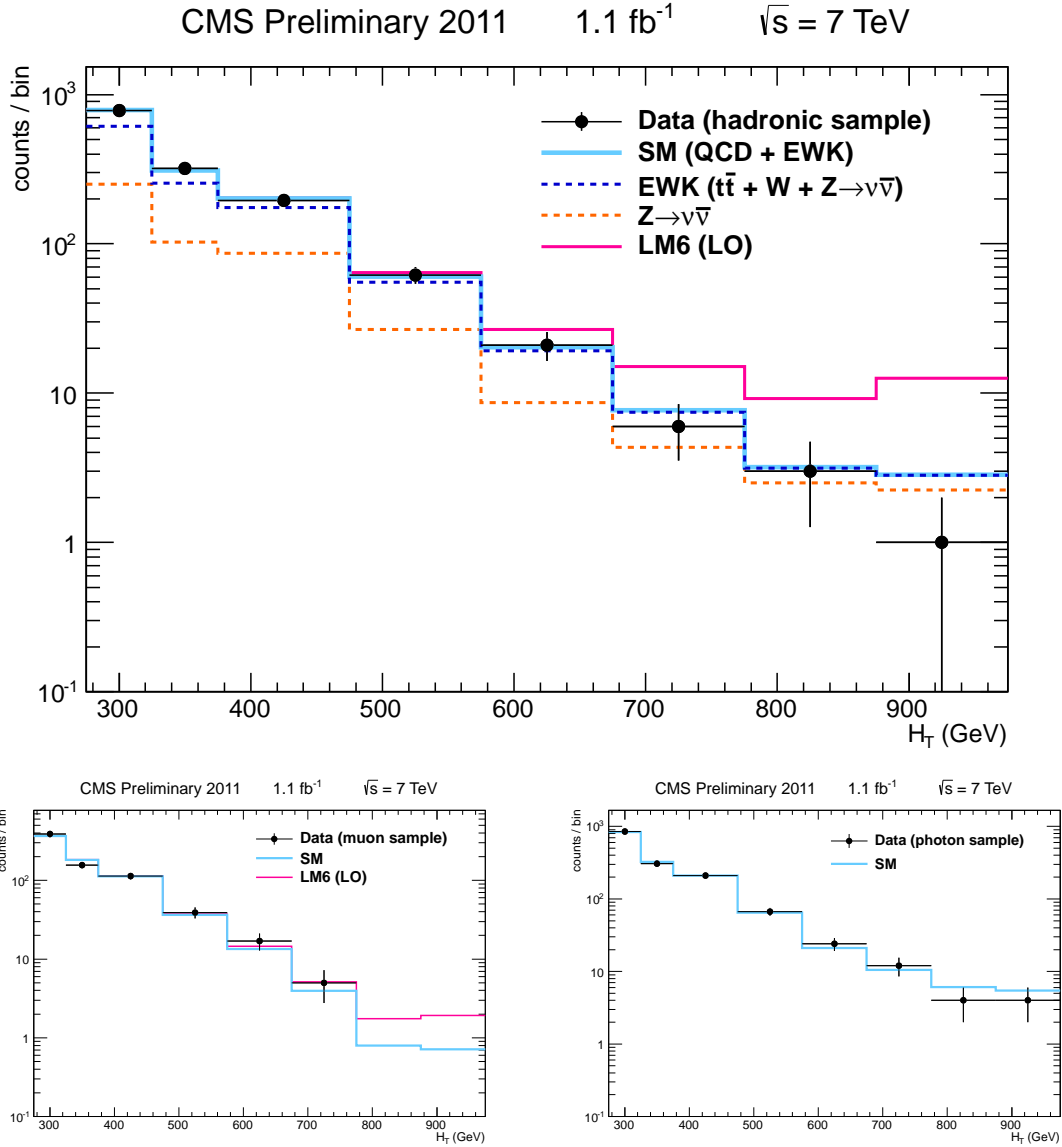


Figure 6.1: Observed yields and fit results in the hadronic (top), muon (bottom left), and photon (bottom right) samples. The signal model LM6 is stacked on the expected background for illustration only; it plays no role in the fit. From [5].

Table 6.2: The maximum-likelihood parameter values under the SM-only hypothesis, and their error estimates as given by HESSE.

parameter	value	error	limits
A_qcd	1.402e-05	$\pm 1.883e-05$	> 0
k_qcd	5.172e-03	$\pm 5.611e-03$	"
A_ewk	1.083e-05	$\pm 1.729e-06$	"
rhoPhotZ	1.081e+00	$\pm 2.557e-01$	"
rhoMuonW	1.145e+00	$\pm 2.149e-01$	"
fZinv0	4.087e-01	$\pm 6.557e-02$	0.2 – 0.8
fZinv1	4.038e-01	$\pm 7.359e-02$	"
fZinv2	4.930e-01	$\pm 7.713e-02$	"
fZinv3	4.809e-01	$\pm 8.306e-02$	"
fZinv4	4.507e-01	$\pm 9.478e-02$	"
fZinv5	5.824e-01	$\pm 1.346e-01$	"
fZinv6	8.000e-01	$\pm 4.491e-01$	"
fZinv7	8.000e-01	$\pm 4.215e-01$	"

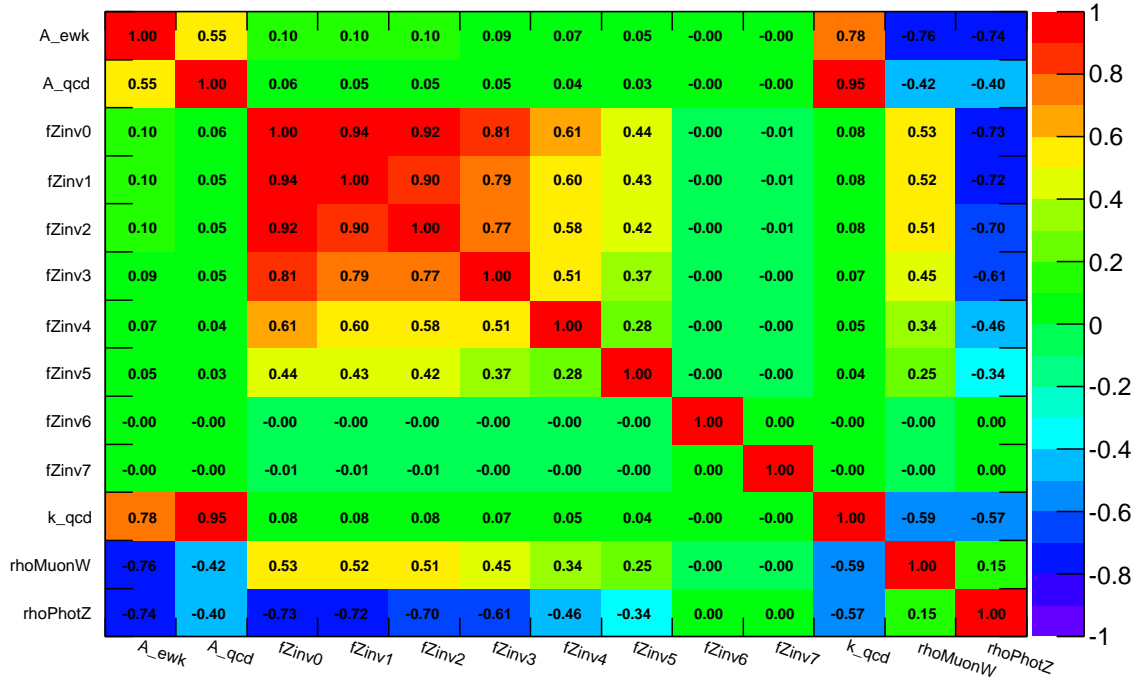


Figure 6.2: The correlation matrix of the fit parameters.

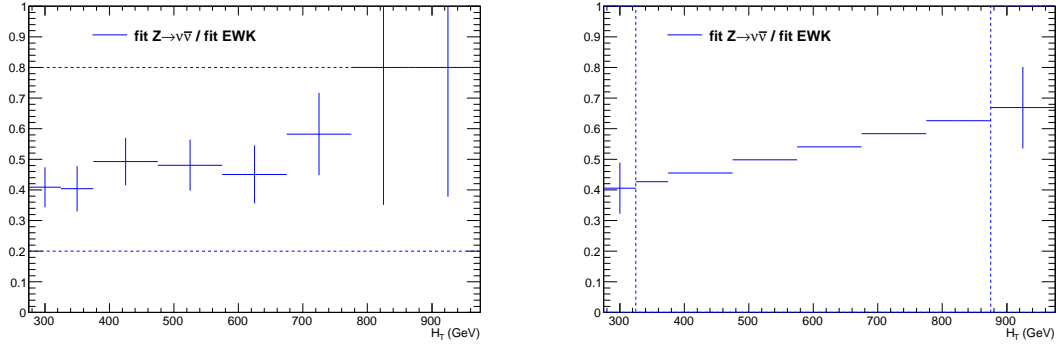


Figure 6.3: Fit results for the fraction of the EWK background which is $Z \rightarrow \nu\bar{\nu}$, *i.e.* the parameters fZ_{inv} . The nominal fit (left) and the alternate fit (right) agree within uncertainties. In the alternate fit, fZ_{inv0} and fZ_{inv7} float, and the intermediate variables are evaluated using linear interpolation.

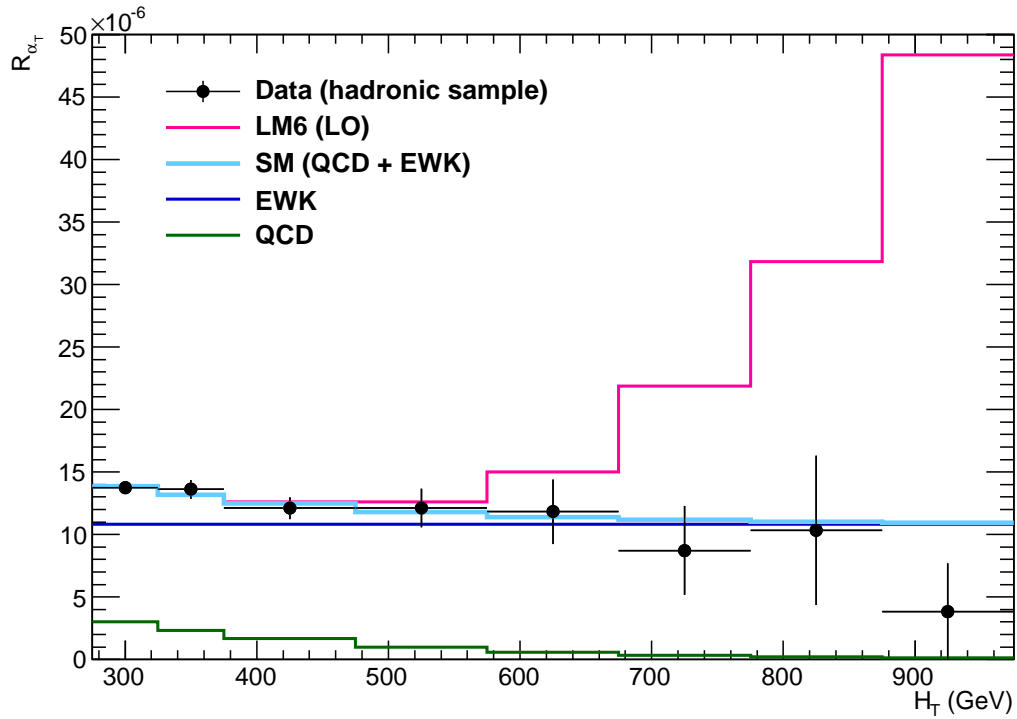


Figure 6.4: Observed yields and ML expectations in the hadronic sample, with LM6 stacked for illustration, all divided by the observed “bulk” yields. Modified from [5].

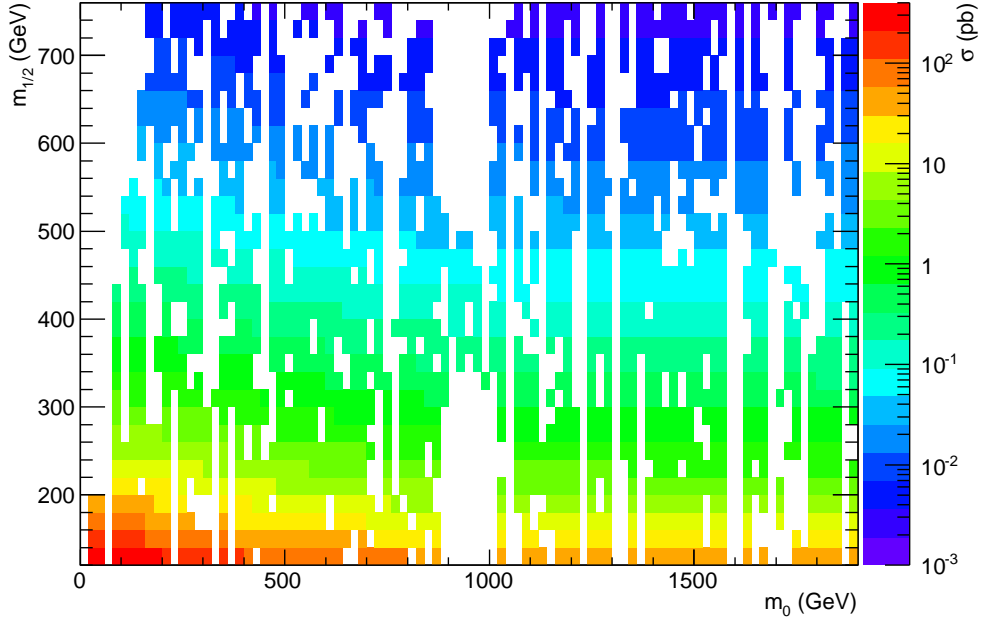


Figure 6.5: The total production cross section as a function of m_0 and $m_{1/2}$ in the specified slice of the CMSSM. Models with coordinates in the white areas were not sampled.

6.2 CMSSM

A model within the CMSSM is specified by four real and one binary parameter, and hence it is not practical to sample a full set of representative values; one needs either further constraints or to choose a subset. In this section, three parameters have been fixed: $\tan\beta = 10$, $A_0 = 0$ GeV, and $\text{sgn}\mu = 1$. m_0 is scanned in steps of 20 GeV up to 2 TeV, and $m_{1/2}$ is scanned steps of 20 GeV up to 800 GeV. At each point, (a) the particle masses are computed using SoftSUSY [79]; (b) the cross section of each scattering process is computed at next-to-leading-order (NLO) using Prospino [80]; (c) 10k events are generated using PYTHIA, fed to the detector simulation and reconstruction chain, and reweighted according to the NLO cross sections. The total production cross section is displayed in Figure 6.5.

The total efficiency of the hadronic selection is shown in Figure 6.6. “Signal

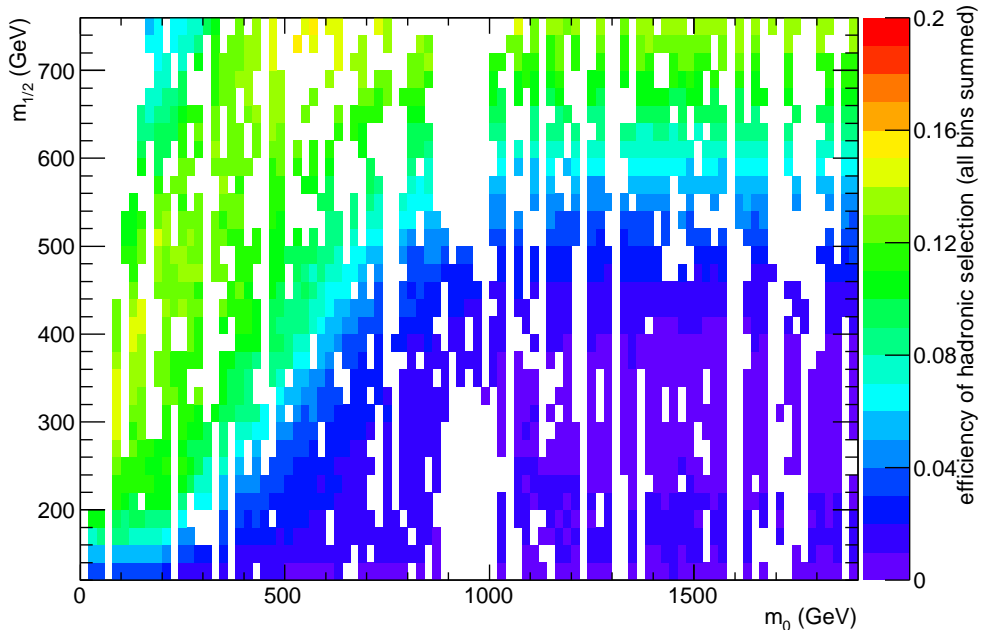


Figure 6.6: The selection efficiency for points in the specified slice of the CMSSM. Models with coordinates in the white areas were not sampled.

contamination” in the muon control sample, though typically only 10–20% of the hadronic efficiency, is taken into account as discussed in Section 5.1.4. Various sources of systematic uncertainty on the signal efficiency are included: uncertainty in the luminosity measurement (6%); potential mis-modeling of the effect of the dead-ECAL-region veto (3%), lepton vetoes (2.5%), and jet energy scale and resolution (2.5%); finite statistics of signal MC (up to a few percent). In addition, the effects of (a) varying the set of parton distribution functions used according to the recommendation of the PDF4LHC working group [81]; (b) changing the renormalization/factorization scale used to compute the cross sections by a factor of two up or down; have been found to affect the efficiency by up to 10%, and are included.

For each point in the grid, the value of CL_s is computed and compared with 0.05 to determine whether the point is excluded by the data, as discussed in Section 5.2. Further, the distribution of CL_s over the SM-only pseudo-experiments is determined, and in particular its 16%, 50%, and 84% quantiles are found. The loci of points at

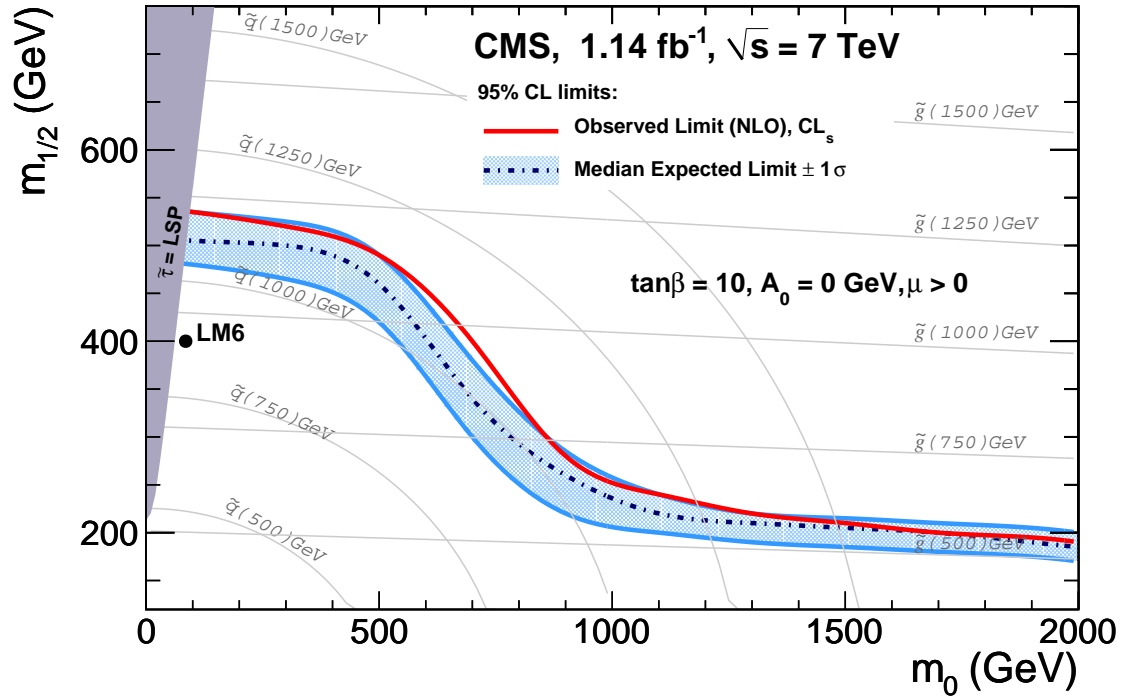


Figure 6.7: Observed and expected limits in the specified slice of the CMSSM; models below the red curve are excluded at 95% C.L. Curves of constant gluino mass and of constant mean u, d, c, s squark masses are drawn as well. In the shaded gray region, the LSP is electrically charged, and hence the models do not exhibit a missing energy signature. From [2].

which these numbers cross 0.05 form the curves shown in Figure 6.7. Interpolation was used to overcome points absent in the scan. For a given value of m_0 , the method has an uncertainty of 10–20 GeV, well within the width of the statistical uncertainty band.

Points with equal gluino and mean u, d, c, s squark mass below approximately 1.1 TeV are excluded at 95% C.L. At higher values of m_0 , where the gluino mass is substantially lower than the mean squark mass, gluino masses below approximately 0.5 TeV are excluded.

6.3 Simplified Models

Though the CMSSM provides a full spectrum of sparticles, the constraints used to define it imply that it cannot represent all possibilities within the MSSM. For example, as visible from the approximate relations between sparticle masses given in Section 1.2, the gluino mass is approximately fixed to six times the lightest neutralino mass.

Simplified Models (SMS), *i.e.* models consisting of only a few sparticles and corresponding free parameters, provide an alternative. Many such models have been proposed [82, 83, 84]. Considered here are two: (a) a model including only a gluino and a neutralino in which gluinos are pair-produced and each undergoes a 3-body decay to a quark, anti-quark, and a neutralino; (b) a model including only a squark, anti-squark and a neutralino, in which the squark and anti-squark are produced together, and each decays to a (anti-)quark and a neutralino. These processes are shown schematically in Figure 1.2.

The masses of the gluino/squark and neutralino are each varied in steps of 25 GeV; for each pair of mass values, 10k events are generated using PYTHIA and fed to the detector simulation and reconstruction chain. The efficiency of the hadronic selection is shown in Figure 6.8. As the parent mass approaches the neutralino mass, the energies of the decay quarks become small, and the analysis efficiency decreases. The systematic uncertainties on the signal efficiency described for the CMSSM models are applied to the simplified models as well. Within these models the yield of signal events in the muon control sample is negligible.

For a given mass pair, an upper limit on the model cross section is computed as described in Section 5.2, *i.e.* the value of the cross section which gives $CL_s = 0.05$ is determined. The limits are shown in Figure 6.9. Further, at each point, the limit is compared to (a) the nominal production cross section of the simplified models computed at next-to-leading-order using Prospino; (b) three times this number; (c) one third of this number. The boundary of the set of points where the cross section

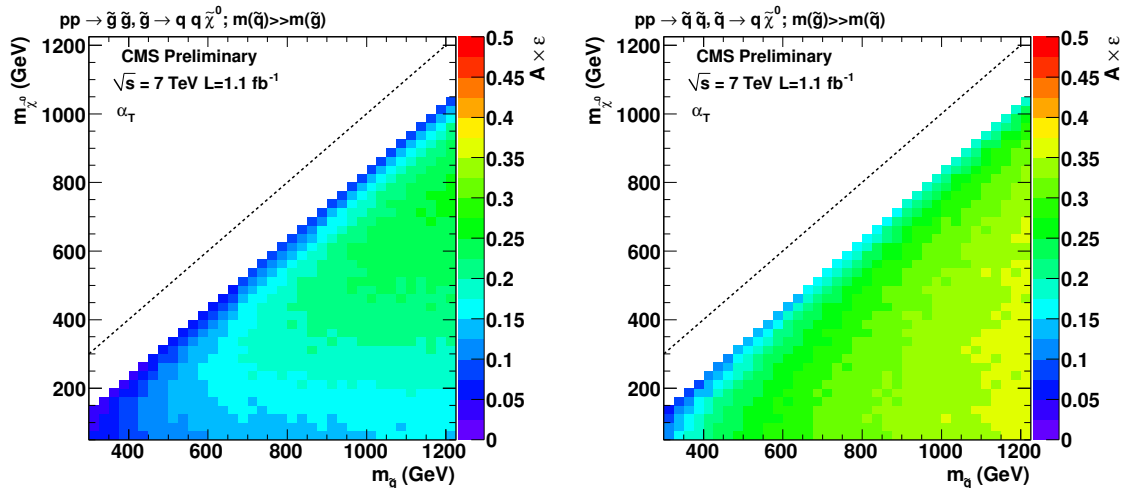


Figure 6.8: The analysis acceptance times efficiency for two simplified models: gluino pairs (left), and squark pairs (right). The dashed lines indicate where the neutralino mass is equal to the gluino mass (left) or squark mass (right). From [5].

limit is lower than the nominal cross section is drawn as a solid curve, and as a dotted (dashed) curve for the higher (lower) cross sections. The cross section variations are intended to indicate the uncertainty in how to apply a cross section limit from a simplified model to a fuller model. For example, squark anti-squark production which proceeds through the exchange of a gluino is not included in the nominal cross section; analogously, the contribution to gluino pair production which proceeds through the exchange of a squark is neglected.

Within the simplified models studied, for an LSP which is approximately 200 GeV lighter than its parent squark or gluino, models with cross sections larger than one to a few picobarns are excluded. For a light LSP, squark (resp. gluino) masses of approximately 700 GeV (resp. 800 GeV) are excluded.

6.4 Summary

The Large Hadron Collider and the Compact Muon Solenoid detector, after tremendous design, construction, and commissioning efforts, have performed superbly in

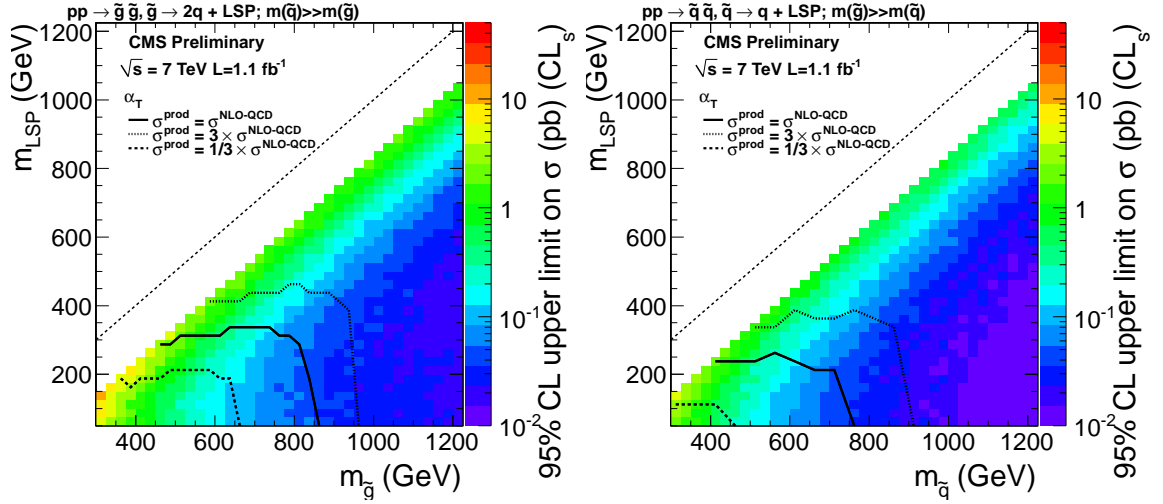


Figure 6.9: 95% C.L. upper limits on cross sections for simplified models: gluino pairs (left); squark pairs (right). The labeled curves indicate where the limit is below a computed cross section for the model. From [5].

their initial run and offered the opportunity to search for new particles and phenomena. Of particular interest are events with observed energetic hadronic showers and also escaping undetected particles, causing an apparent imbalance of particle momenta. If observed at rates not explained by known processes, such events could provide substantial clues about what physics may lie beyond the Standard Model.

Despite its potential, an all-hadronic search for escaping particles at a proton-proton collider presents a challenge. One infers the momenta of invisible particles from those of the observed particles, and in doing so removes redundancy from the measurement of an event. One is exposed to instrumental difficulties such as spurious noise, detection inefficiency, and reconstruction failures. One samples extreme tails of strong multi-jet production, *e.g.*, jets which saturate channels or punch through the calorimetry, or multiple low- p_T jets azimuthally aligned. In addition, one lacks in the signal selection a clean handle, *e.g.* an isolated lepton, in both the trigger and in the offline analysis.

Presented is a search which has powerful rejection of mis-measured multi-jet events. In particular, a novel kinematic variable, α_T , provides discrimination be-

tween events with fake and genuine missing transverse energy. Constraints on the remaining background rates are driven by data control samples. The observations are found to agree with expectations from the Standard Model, and the results are interpreted within two classes of supersymmetric models— the Constrained Minimal Supersymmetric Standard Model and Simplified Models— where many plausible models are found to be incompatible with the data. At the time of writing, these are the most stringent published limits on such models from a collider.

Bibliography

- [1] V. Khachatryan *et al.*, “Search for Supersymmetry in pp Collisions at 7 TeV in Events with Jets and Missing Transverse Energy,” *Phys.Lett.* B698 (2011) 196–218, [arXiv:1101.1628](#).
- [2] S. Chatrchyan *et al.*, “Search for Supersymmetry at the LHC in Events with Jets and Missing Transverse Energy,” *Phys.Rev.Lett.* 107 (2011) 221804, [arXiv:1109.2352](#).
- [3] CMS Collaboration, “Search for Supersymmetry in the Jets and Missing Energy Final State in pp collisions at 7 TeV,” 2010. CMS Physics Analysis Summary SUS-10-003.
- [4] CMS Collaboration, “Further interpretation of the search for supersymmetry based on α_T ,” 2011. CMS Physics Analysis Summary SUS-11-001.
- [5] CMS Collaboration, “Search for supersymmetry in all-hadronic events with α_T ,” 2011. CMS Physics Analysis Summary SUS-11-003.
- [6] S. Glashow, “Partial Symmetries of Weak Interactions,” *Nucl.Phys.* 22 (1961) 579–588.
- [7] S. Weinberg, “A Model of Leptons,” *Phys.Rev.Lett.* 19 (1967) 1264–1266.
- [8] A. Salam, “Weak and Electromagnetic Interactions,” *Conf.Proc.* C680519 (1968) 367–377.

- [9] H. Politzer, “Reliable Perturbative Results for Strong Interactions?,” *Phys.Rev.Lett.* 30 (1973) 1346–1349.
- [10] D. Gross and F. Wilczek, “Ultraviolet Behavior of Nonabelian Gauge Theories,” *Phys.Rev.Lett.* 30 (1973) 1343–1346.
- [11] F. Halzen and A. D. Martin, *Quarks and leptons: an introductory course in modern particle physics*. Wiley, New York, NY, 1984.
- [12] G. Altarelli and K. Winter, *Neutrino mass*. Springer tracts in modern physics. Springer, Berlin, 2003.
- [13] J. Branson *et al.*, “High transverse momentum physics at the Large Hadron Collider: The ATLAS and CMS Collaborations,” *Eur.Phys.J.direct* C4 (2002) N1, [arXiv:hep-ph/0110021](#).
- [14] K. Nakamura *et al.*, “Review of particle physics,” *J.Phys.G* G37 (2010) 075021.
- [15] M. S. Carena and H. E. Haber, “Higgs boson theory and phenomenology,” *Prog.Part.Nucl.Phys.* 50 (2003) 63–152, [arXiv:hep-ph/0208209](#).
- [16] Y. Golfand and E. Likhtman, “Extension of the Algebra of Poincare Group Generators and Violation of p Invariance,” *JETP Lett.* 13 (1971) 323–326.
- [17] J. Wess and B. Zumino, “Supergauge transformations in four dimensions,” *Nucl. Phys.* B70 (1974) 39.
- [18] H. P. Nilles, “Supersymmetry, supergravity and particle physics,” *Phys. Reports* 110 (1984) 1.
- [19] H. E. Haber and G. L. Kane, “The search for supersymmetry: Probing physics beyond the standard model,” *Phys. Reports* 117 (1987) 75.

- [20] R. Barbieri, S. Ferrara, and C. A. Savoy, “Gauge Models with Spontaneously Broken Local Supersymmetry,” *Phys. Lett.* B119 (1982) 343.
- [21] S. Dawson, E. Eichten, and C. Quigg, “Search for Supersymmetric Particles in Hadron - Hadron Collisions,” *Phys. Rev.* D31 (1985) 1581.
- [22] E. Witten, “Dynamical Breaking of Supersymmetry,” *Nucl.Phys.* B188 (1981) 513.
- [23] S. Dimopoulos and H. Georgi, “Softly Broken Supersymmetry and SU(5),” *Nucl.Phys.* B193 (1981) 150.
- [24] G. Jungman, M. Kamionkowski, and K. Griest, “Supersymmetric dark matter,” *Phys.Rept.* 267 (1996) 195–373, [arXiv:hep-ph/9506380](https://arxiv.org/abs/hep-ph/9506380).
- [25] S. P. Martin, “A Supersymmetry primer,” [arXiv:hep-ph/9709356](https://arxiv.org/abs/hep-ph/9709356).
- [26] G. R. Farrar and P. Fayet, “Phenomenology of the Production, Decay, and Detection of New Hadronic States Associated with Supersymmetry,” *Phys. Lett.* B76 (1978) 575.
- [27] S. Dimopoulos and D. W. Sutter, “The Supersymmetric flavor problem,” *Nucl.Phys.* B452 (1995) 496–512, [arXiv:hep-ph/9504415](https://arxiv.org/abs/hep-ph/9504415).
- [28] G. L. Kane, C. F. Kolda, L. Roszkowski, and J. D. Wells, “Study of constrained minimal supersymmetry,” *Phys.Rev.* D49 (1994) 6173–6210, [arXiv:hep-ph/9312272](https://arxiv.org/abs/hep-ph/9312272).
- [29] A. H. Chamseddine, R. L. Arnowitt, and P. Nath, “Locally Supersymmetric Grand Unification,” *Phys.Rev.Lett.* 49 (1982) 970.
- [30] K. Inoue, A. Kakuto, H. Komatsu, and S. Takeshita, “Aspects of Grand Unified Models with Softly Broken Supersymmetry,” *Prog.Theor.Phys.* 68 (1982) 927.

- [31] S. Abdullin *et al.*, “Discovery potential for supersymmetry in CMS,” *J.Phys.G* G28 (2002) 469, [arXiv:hep-ph/9806366](https://arxiv.org/abs/hep-ph/9806366).
- [32] G. Bayatian *et al.*, “CMS technical design report, volume II: Physics performance,” *J.Phys.G* G34 (2007) 995–1579.
- [33] CMS Collaboration.
<https://twiki.cern.ch/twiki/bin/viewauth/CMS/SUSYMassSpectra>.
- [34] L. Evans and P. Bryant, “LHC Machine,” *JINST* 3 (2008) S08001.
- [35] J.-L. Caron, “LHC Layout.” CERN LHC Project Illustrations, Sep, 1997.
- [36] CMS Collaboration, “CMS Luminosity - Public Results.”
<https://twiki.cern.ch/twiki/bin/view/CMSPublic/LumiPublicResults>.
- [37] R. K. Ellis, W. J. Stirling, and B. R. Webber, *QCD and Collider Physics*.
Cambridge monographs on particle physics, nuclear physics, and cosmology.
Cambridge Univ. Press, Cambridge, 2003. Photography by S. Vascotto.
- [38] J. Stirling, “Cross section plots.”
<http://www.hep.phy.cam.ac.uk/~wjs/plots/plots.html>.
- [39] T. Plehn, “Prospino2 results.” <http://www.thphys.uni-heidelberg.de/~plehn/index.php?show=prospino>.
- [40] R. Adolphi *et al.*, “The CMS experiment at the CERN LHC,” *JINST* 3 (2008) S08004.
- [41] CMS Collaboration, “Performance of muon identification in pp collisions at $\sqrt{s} = 7$ TeV,” 2010. CMS Physics Analysis Summary MUO-10-002.

- [42] CMS Collaboration, “Absolute Calibration of the CMS Luminosity Measurement: Summer 2011 Update,” 2011. CMS Physics Analysis Summary EWK-11-001.
- [43] G. Bayatian *et al.*, “CMS physics: Technical design report,” 2006. CERN-LHCC-2006-001, CMS-TDR-008-1.
- [44] M. Cacciari, G. P. Salam, and G. Soyez, “The Anti-k(t) jet clustering algorithm,” *JHEP* 0804 (2008) 063, [arXiv:0802.1189](#).
- [45] S. Chatrchyan *et al.*, “Determination of Jet Energy Calibration and Transverse Momentum Resolution in CMS,” *JINST* 6 (2011) P11002, [arXiv:1107.4277](#).
- [46] S. Chatrchyan *et al.*, “Missing transverse energy performance of the CMS detector,” *JINST* 6 (2011) P09001, [arXiv:1106.5048](#).
- [47] P. M. Nadolsky, H.-L. Lai, Q.-H. Cao, J. Huston, J. Pumplin, *et al.*, “Implications of CTEQ global analysis for collider observables,” *Phys.Rev.* D78 (2008) 013004, [arXiv:0802.0007](#).
- [48] J. Alwall, P. Demin, S. de Visscher, R. Frederix, M. Herquet, *et al.*, “MadGraph/MadEvent v4: The New Web Generation,” *JHEP* 0709 (2007) 028, [arXiv:0706.2334](#).
- [49] T. Sjostrand, S. Mrenna, and P. Z. Skands, “PYTHIA 6.4 Physics and Manual,” *JHEP* 0605 (2006) 026, [arXiv:hep-ph/0603175](#).
- [50] S. Agostinelli *et al.*, “GEANT4: A Simulation toolkit,” *Nucl.Instrum.Meth.* A506 (2003) 250–303.
- [51] K. Melnikov and F. Petriello, “Electroweak gauge boson production at hadron colliders through $O(\alpha(s)^2)$,” *Phys. Rev.* D74 (2006) 114017, [arXiv:hep-ph/0609070](#).

- [52] CMS Collaboration. <https://twiki.cern.ch/twiki/bin/viewauth/CMS/StandardModelCrossSections>.
- [53] CMS Collaboration. <https://twiki.cern.ch/twiki/bin/view/CMSPublic/SWGuideFastSimulation>.
- [54] LHC Project, “LHC Modes.”
<http://lhc-commissioning.web.cern.ch/lhc-commissioning/systems/data-exchange/doc/LHC-OP-ES-0005-10-00.pdf>. LHC-OP-ES-0005.
- [55] O. S. Brüning, P. Collier, P. Lebrun, S. Myers, R. Ostojic, J. Poole, and P. Proudlock, *LHC Design Report*. CERN, Geneva, 2004. Section 19.3, Interfaces with the Experiments.
- [56] S. Chatrchyan *et al.*, “Identification and Filtering of Uncharacteristic Noise in the CMS Hadron Calorimeter,” *JINST* 5 (2010) T03014, [arXiv:0911.4881](https://arxiv.org/abs/0911.4881).
- [57] CMS Collaboration, “Electron reconstruction and identification at $\sqrt{s} = 7$ TeV,” 2010. CMS Physics Analysis Summary EGM-10-004.
- [58] CMS Collaboration, “Electron Identification Based on Simple Cuts.”
<https://twiki.cern.ch/twiki/bin/viewauth/CMS/SimpleCutBasedEleID>.
- [59] S. Chatrchyan *et al.*, “Search for Supersymmetry in pp Collisions at $\sqrt{s} = 7$ TeV in Events with Two Photons and Missing Transverse Energy,” *Phys. Rev. Lett.* 106 (2011) 211802, [arXiv:1103.0953](https://arxiv.org/abs/1103.0953).
- [60] CMS Collaboration, “Search for Supersymmetry in Events with Photons, Jets and Missing Energy,” 2011. CMS Physics Analysis Summary SUS-11-009.
- [61] CMS Collaboration, “Calorimeter Jet Quality Criteria for the First CMS Collision Data,” <http://cdsweb.cern.ch/record/1259924>. CMS Physics Analysis Summary JME-09-008.

- [62] L. Randall and D. Tucker-Smith, “Dijet Searches for Supersymmetry at the LHC,” *Phys.Rev.Lett.* 101 (2008) 221803, [arXiv:0806.1049](#).
- [63] CMS Collaboration, “SUSY searches with dijet events,” 2008. CMS Physics Analysis Summary SUS-08-005.
- [64] CMS Collaboration, “Search strategy for exclusive multi-jet events from supersymmetry at CMS,” 2009. CMS Physics Analysis Summary SUS-09-001.
- [65] V. Khachatryan *et al.*, “First Measurement of the Cross Section for Top-Quark Pair Production in Proton-Proton Collisions at $\sqrt{s}=7$ TeV,” *Phys.Lett.* B695 (2011) 424–443, [arXiv:1010.5994](#).
- [66] Z. Bern, G. Diana, L. Dixon, F. Febres Cordero, S. Hoche, *et al.*, “Driving Missing Data at Next-to-Leading Order,” *Phys.Rev.* D84 (2011) 114002, [arXiv:1106.1423](#).
- [67] CMS Collaboration, “Data-Driven Estimation of the Invisible Z Background to the SUSY MET Plus Jets Search,” 2008. CMS Physics Analysis Summary SUS-08-002.
- [68] CMS Collaboration, “Photon ID Task Force.”
<https://twiki.cern.ch/twiki/bin/view/CMS/PhotonID>.
- [69] CMS Collaboration, “Isolated Photon Reconstruction and Identification at $\sqrt{s} = 7$ TeV,” 2010. CMS Physics Analysis Summary EGM-10-006.
- [70] CMS Collaboration, “Electromagnetic calorimeter commissioning and performance with 7 TeV data,” 2010. CMS Physics Analysis Summary EGM-10-002.
- [71] L. Dixon, private communication.

- [72] V. Khachatryan *et al.*, “Measurements of Inclusive W and Z Cross Sections in pp Collisions at $\sqrt{s}=7$ TeV,” *JHEP* 01 (2011) 080, [arXiv:1012.2466](#).
- [73] S. Chatrchyan *et al.*, “Measurement of the t t-bar production cross section and the top quark mass in the dilepton channel in pp collisions at $\sqrt{s} = 7$ TeV,” *JHEP* 07 (2011) 049, [arXiv:1105.5661](#).
- [74] A. L. Read, “Modified frequentist analysis of search results (The CL(s) method),” 2000. CERN-OPEN-2000-205.
- [75] G. Cowan, K. Cranmer, E. Gross, and O. Vitells, “Asymptotic formulae for likelihood-based tests of new physics,” *Eur.Phys.J. C* 71 (2011) 1554, [arXiv:1007.1727](#).
- [76] W. Verkerke and D. Kirkby, “RooFit.”
<http://root.cern.ch/drupal/content/roofit>.
- [77] F. James and M. Roos, “Minuit: A System for Function Minimization and Analysis of the Parameter Errors and Correlations,” *Comput.Phys.Commun.* 10 (1975) 343–367.
- [78] G. D. Cowan, *Statistical data analysis*. Oxford Univ. Press, Oxford, 1998.
- [79] B. Allanach, “SOFTSUSY: a program for calculating supersymmetric spectra,” *Comput.Phys.Commun.* 143 (2002) 305–331, [arXiv:hep-ph/0104145](#).
- [80] W. Beenakker, R. Hopker, M. Spira, and P. Zerwas, “Squark and gluino production at hadron colliders,” *Nucl.Phys. B* 492 (1997) 51–103, [arXiv:hep-ph/9610490](#).
- [81] M. Botje, J. Butterworth, A. Cooper-Sarkar, A. de Roeck, J. Feltesse, *et al.*, “The PDF4LHC Working Group Interim Recommendations,” [arXiv:1101.0538](#).

- [82] J. Alwall, P. Schuster, and N. Toro, “Simplified Models for a First Characterization of New Physics at the LHC,” *Phys. Rev. D* 79 (2009) 075020, [arXiv:0810.3921](#).
- [83] J. Alwall, M.-P. Le, M. Lisanti, and J. G. Wacker, “Model-Independent Jets plus Missing Energy Searches,” *Phys.Rev. D* 79 (2009) 015005, [arXiv:0809.3264](#).
- [84] D. Alves, N. Arkani-Hamed, S. Arora, Y. Bai, M. Baumgart, *et al.*, “Simplified Models for LHC New Physics Searches,” [arXiv:1105.2838](#).

Index

- α_T , 28
- CL_s , 55
- CMS, 14
- CMSSM, 6, 63
- ΔR , 26
- electron, 19
- E_T , *see* transverse energy
- \cancel{E}_T , *see* missing transverse energy
- η , *see* pseudo-rapidity
- event, 17
- gluino, 4
- hit, 18
- H_T , 23
- jet, 13, 19
- lepton, 2
- LM benchmark points, 22
- LSP, 5
- luminosity, 11
- maximum likelihood, 56
- MC, *see* Monte Carlo
- missing transverse energy, 20
- ML, *see* maximum likelihood
- Monte Carlo, 20
- MSSM, 4
- muon, 19
- neutralino, 5
- parton, 12
- photon, 19
- pile-up, 13
- pseudo-rapidity, 13
- quark, 2
- Simplified Models, 66
- SM, *see* Standard Model
- SMS, *see* Simplified Models
- sparticle, 4
- squark, 4
- Standard Model, 2
- track, 19
- transverse energy, 13
- trigger, 17
- vertex, 19